Monthly Notices of the ROYAL ASTRONOMICAL SOCIETY

MNRAS **514,** 1315–1334 (2022) https://doi.org/10.1093/mnras/stac1100
Advance Access publication 2022 April 30

Estimating transient rates from cosmological simulations and BPASS

Max M. Briel [1]★, J. J. Eldridge [1], Elizabeth R. Stanway [2], H. F. Stevance [1] and A. A. Chrimes [3]

[1]*Department of Physics, University of Auckland, Private Bag 92019, Auckland, New Zealand*
[2]*Department of Physics, University of Warwick, Gibbet Hill Road, Coventry CV4 7AL, UK*
[3]*Department of Astrophysics/IMAPP, Radboud University, PO Box 9010, NL-6500 GL, the Netherlands*

Accepted 2022 April 8. Received 2022 March 28; in original form 2021 November 13

ABSTRACT

The detection rate of electromagnetic (EM) and gravitational wave (GW) transients is growing exponentially. As the accuracy of the transient rates will significantly improve over the coming decades, so will our understanding of their evolution through cosmic history. To this end, we present predicted rates for EM and GW transients over the age of the universe using Binary Population and Spectral Synthesis (BPASS) results combined with four cosmic star formation histories (SFHs). These include a widely used empirical SFH of Madau & Dickinson and those from three cosmological simulations: MilliMillennium, EAGLE, and IllustrisTNG. We find that the choice of SFH changes our predictions: transients with short delay times are most affected by the star formation rate and change up to a factor of 2, while long delay time events tend to depend on the metallicity evolution of star formation and can change the predicted rate up to an order of magnitude. Importantly, we find that the cosmological simulations have very different metallicity evolution that cannot be reproduced by the widely used metallicity model of Langer & Norman, which impacts the binary black hole merger, stripped-envelope supernovae, and LGRBs in the local Universe most acutely. We recommend against using simple prescriptions for the metallicity evolution of the universe when predicting the rates of events that can have long delay times and that are sensitive to metallicity evolution.

Key words: stars: massive – black hole mergers – black hole - neutron star mergers – neutron star mergers – gamma-ray bursts – transients: supernovae.

1 INTRODUCTION

Astrophysical transients are central to our understanding of stellar populations due to their dependence on the evolutionary history of the progenitor stars. Transient studies, therefore, probe distinct evolutionary and environmental parameters, although subject to model uncertainties. Commonly observed events are electromagnetic transients, which include supernovae (SNe), their many SNe subtypes, Long Gamma-Ray Bursts (LGRB), and Pair-Instability SNe (PISNe), while the gravitational wave (GW) transients comprise BHNS, binary black hole (BBH), and binary neutron star (BNS) mergers, with the latter also producing an electromagnetic signal, known as a short gamma-ray burst (Abbott et al. 2017).

Predicting cosmic transient rates is an essential test for population synthesis codes and provides insight into the underlying stellar population producing these short-lived astrophysical events. To perform these predictions, environment and stellar evolution prescriptions are required. The influence of the former on transient rates has started to be considered in detail in the last few years and primarily focuses on GW transients (Belczynski et al. 2018; Giacobbo & Mapelli 2018; Kruckow et al. 2018; Chruslinska & Nelemans 2019; Chruslinska, Nelemans & Belczynski 2019; Belczynski et al. 2020; du Buisson et al. 2020; Tang et al. 2020; Santoliquido et al. 2020a). It describes the amount of stellar material formed (cosmic star formation rate density; CSFRD) and metallicity evolution over the history of the Universe. Traditionally, the CSFRD is an empirical fit to volume-averaged UV and IR observations (Behroozi, Wechsler & Conroy 2013; Madau & Dickinson 2014; Madau & Fragos 2017) averaging out the effects of cosmic variance due to large scale structures. It is well measured up to a redshift of 8, with limited observations going up to $z = 10$. At lower redshifts further constraints on the empirical cosmic star formation history (SFH) can be obtained, such as using radio (Karim et al. 2011; Matthews et al. 2021), 24 micron (Rodighiero et al. 2010) or, most commonly, H α (Gilbank et al. 2010) observations, which find similar results to UV and IR estimates.

The second component of the environment prescriptions (the metallicity) consists of an average cosmic metallicity evolution, a mass function, and mass–metallicity correlations, which are combined to give a fractional mass density per metallicity over redshift, as described in Langer & Norman (2006). Each component is empirically fitted using different techniques from emission-line studies to deep sky surveys. Moreover, it is widely used in population synthesis studies of GW transients, and modified and tested against GW transient rates by Neijssel et al. (2019).

The combination of CSFRD and metallicity evolution provides a metallicity-specific cosmic SFH that conforms to observations, but it misses the details of at the scale of individual galaxies and is subject to observational biases and sparse data. This additional level of detail can be provided by cosmological simulations, which produce SFHs and metallicity evolution on a per galaxy basis, though subject to the assumed input physics and numerical limits. As a

★ E-mail: max.briel@gmail.com

result, cosmological simulations have been extensively used to look at the relations between host galaxies and GW transients (Mapelli et al. 2017, 2019; Belczynski et al. 2018; Mapelli & Giacobbo 2018; Artale et al. 2019, 2020; Toffano et al. 2019; Chu, Yu & Lu 2021). And with improvements to the input physics and output resolution in recent years, cosmological simulations reproduce many observational relations, such as the CSFRD and galaxy colour bimodality at low redshift (Nelson et al. 2018).

The stellar prescription for predicting cosmic transients is encompassed in the physics of a population synthesis code and needs to cover a broad mass range and binary configurations due to the variety in transient progenitors. The influence of the implemented evolutionary physics on the compact object merger rate has been explored using rapid population synthesis codes (see Han et al. 2020; Mandel & Broekgaarden 2021; and references therein). Such codes allow for the exploration of a vast evolutionary parameter space using a variety of models and analytical fits, but therefore is limited in the inclusion of computationally intensive detailed stellar structures, which can alter the outcome of binary interactions (Gallegos-Garcia et al. 2021; Marchant et al. 2021).

We use the detailed models from Binary Population And Spectral Synthesis (BPASS; Eldridge et al. 2017; Stanway & Eldridge 2018) to predict electromagnetic and GW transient rates from a single population. This allows transient rates to provide additional constraints on other rates, as shown by Bavera et al. (2021a) for LGRBs and BBH mergers. Similar to Eldridge, Stanway & Tang (2019), we combine these rates with an SFH to extract the cosmic event rate density. But instead of using an empirical CSFRD and metallicity description, we extract detailed SFHs and metallicity evolution from the EAGLE (Schaye et al. 2015; Crain et al. 2015), IllustrisTNG (Springel et al. 2018; Nelson et al. 2018; Pillepich et al. 2018b; Naiman et al. 2018; Marinacci et al. 2018), and MilliMillennium (Springel et al. 2005) simulations. While uncertainty from the assumed stellar physics, such as the SN explosion mechanism, mass transfer, and stellar winds, remains, we put the most robust and self-consistent constraints to date on the population synthesis physics and the star formation environment by predicting all transients from these different synthetic stellar populations.

Section 2 discusses the population synthesis of BPASS and electromagnetic and GW transients it predicts. The empirical and cosmological simulation SFHs discussed in section 3 and are combined in section 4 with the BPASS predictions to extract cosmic transient rates. We discuss the volume-averaged transient rates and compare them against observations in Section 5. Section 6 puts the work in the context of other results, combines the rates, and Section 7 concludes with a brief summary of our results.

2 BINARY POPULATION SYNTHESIS

The BPASS v2.2.1 models (Eldridge et al. 2017; Stanway & Eldridge 2018) comprise of a grid of from 0.1 to 300 $M_\odot$ 1D theoretical stellar models with single and binary star evolution, created using an adapted version of the Cambridge STARS code (Eggleton 1971). It includes metallicity-dependent mass-loss rates for stellar winds from de Jager, Nieuwenhuijzen & van der Hucht (1988), except for OB stars and hydrogen depleted Wolf–Rayet stars for which, respectively, prescriptions from Vink, de Koter & Lamers (2001) and Nugis & Lamers (2000) are used. In the initial phase of the binary evolution, the primary is evolved in detail, while the secondary is evolved using the single star rapid evolution equations from Hurley, Tout & Pols (2002). Once the evolutionary outcome of the primary has been decided, the secondary model is switched out for a detailed single star model or a detailed binary system with compact remnant depending on the outcome of the primary.

During the lifetime of the binary system, either star can fill their Roche Lobe and transfer material to their companion. The mass-loss rate due to this overflow is determined by the radius of the donor and Roche Lobe radius as described in Eldridge et al. (2017). For stellar companions, the thermal time-scale limits the accretion rate to $\dot{M}_2 \leq M_2/\tau_{\rm KH}$, while for compact remnants the accretion rate is limited to the Eddington luminosity for masses below $3\,M_\odot$ (for more details, see Eldridge, Izzard & Tout 2008) and unrestricted for masses above this, allowing for super-Eddington accretion. Any remaining mass is lost to the system together with its orbital angular momentum treating this as a wind from the donor star. If, during the mass transfer, the radius of the donor continues to grow to the binary separation, a common envelope is formed of which the outcome is determined by comparing the binding energy against the orbital energy (Ivanova et al. 2013).

The grid of models is weighted using a Kroupa (2001) initial mass function extended to $300\,M_\odot$ and initial binary parameters from empirical distributions (Moe & Di Stefano 2017), creating a population with known mass and age. The grid of stellar models contains 13 metallicities ranging from $Z = 10^{-5}$ to 0.04 with $Z = 0.020$ considered Solar metallicity.

A vital benefit of the detailed stellar models is the access to the star's structure at the end of its life, which provides a systematic method to predict the subsequent transient. An extensive definition of the transient definitions in BPASS can be found in Eldridge et al. (2013, 2017), here we provide a short overview of the criteria.

Massive stars ($M \gtrsim 8\,M_\odot$) end their life in an explosion caused by the collapse of the stellar core, appropriately named a Core-Collapse SN (CCSN) (e.g. Heger et al. 2003; Smartt et al. 2009). BPASS classifies CCSN progenitors as stars that have a carbon–oxygen core above $1.38\,M_\odot$, and have a final stellar mass above $1.5\,M_\odot$. These models have undergone carbon burning and generate a oxygen–neon core capable of collapsing resulting in an SN (Tout 2011).

From an observational point of view, CCSNe are divided into subtypes based on their spectra; Type II SNe are hydrogen-rich, while Types Ib and Ic lack hydrogen completely but exhibit either the presence or absence, respectively, of helium (Filippenko 1997). Within BPASS, the elemental abundances in the ejecta mass are a proxy to determine the subtype of the CCSN (Eldridge, Langer & Tout 2011; Eldridge et al. 2013, 2017). The parameters were chosen for each CCSN subtype to match the observed local relative rates within ∼20 Mpc (Eldridge et al. 2013) and the Ib to Ic relative rate in Shivvers et al. (2017). Multiple formation pathways contribute to each of the progenitors; for example, an envelope can be removed by strong stellar winds (Woosley, Heger & Weaver 2002; Heger et al. 2003), stable mass transfer with a binary companion, or the explosion of a companion (Paczyński 1971; Podsiadlowski, Joss & Hsu 1992; De Donder & Vanbeveren 1998; Vanbeveren, De Loore & Van Rensbergen 1998; Smith et al. 2011). The CCSNe progenitors that have lost most or all of their hydrogen envelope are also known as stripped-envelope SNe (SESNe) and are likely to originate from binary systems (Yoon, Woosley & Langer 2010; Yoon 2015). During some SESNe, a relativistic jet is launched, and its interaction with the stellar envelope or the surrounding medium can excite high-energy emission, detectable as an LGRB (e.g. Heger et al. 2003; Langer 2012). BPASS only considers LGRB formation through chemically homogeneous evolution through fast rotation and mixing caused by low metallicity mass transfer. If the star's evolution leads to a CCSN with a remnant mass greater than $3\,M_\odot$, it is classified as an LGRB in

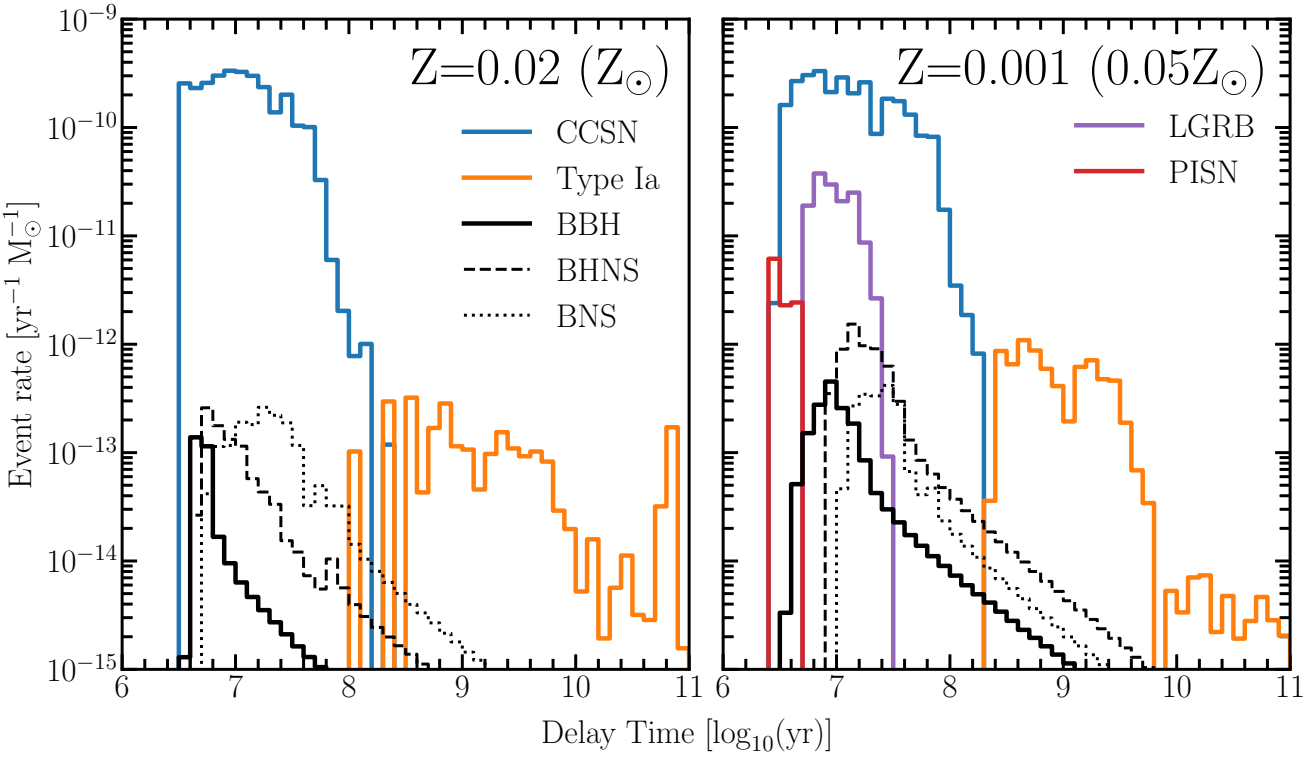

Figure 1. The distribution of event rates over time from stellar birth to the specific transient for metallicities $Z = Z_{\odot}$ (left) and $Z = 0.05\,Z_{\odot}$ (right).

BPASS. Tidal and magnetar-induced GRBs are added through post-processing by models from Chrimes, Stanway & Eldridge (2020).

At the end of their main-sequence evolution, extremely massive stars ($M \gtrsim 100 - 130\,M_{\odot}$) have a low-density, high-temperature helium core. This combination gives rise to electron–positron pair production and removes the radiative pressure that keeps the star from collapsing. This can lead to a pulsation pair-instability SN, where the star can ejects up to several solar masses in pulses, before possibly returning to a regime where electron–positron pair production is no longer possible (Woosley 2017). If, instead, the helium core is above $64\,M_{\odot}$ a pair-instability SN (PISN) completely disrupts the star, and no remnant is left behind (Fowler & Hoyle 1964; Rakavy & Shaviv 1967; Heger & Woosley 2002). While the exact mass range is uncertain (Farmer et al. 2019; Woosley & Heger 2021; and references therein), BPASS defines a PISN progenitor as a star with a helium core mass between 64 and $133\,M_{\odot}$, but does not consider pulsation pair-instability SNe. Observationally no confident detection has been made, but several Super-Luminous SNe Type I (SLSNe-I) have been identified as possible candidates (Woosley, Blinnikov & Heger 2007; Gal-Yam et al. 2009; Cooke et al. 2012; Terreran et al. 2017; Gomez et al. 2019).

Like some SESNe, Type Ia SNe also lack hydrogen in their spectra but are not the result of a core-collapse. Instead, they originate from binary progenitors that involve an electron-degenerate white dwarf. This star gains mass from a main-sequence companion (single-degenerate channel) or merges with another white dwarf through the emission of GWs (double-degenerate channel). If, as a result of the added mass, the white dwarf approaches or exceeds the Chandrasekhar limit of $1.4M_{\odot}$, a thermonuclear explosion occurs (e.g. Howell 2011; Maoz, Mannucci & Nelemans 2014). Besides being the main driving force behind the Type Ia double-degenerate formation pathway, the loss of orbital energy through GW emission also drives the decrease in orbital separation and merger of other double compact object systems, such as BNS, black hole-neutron star (BHNS), and binary black hole (BBH) systems. Seconds before the merger, an increase in GW frequency and amplitude allows for measurement of this chirp event using the LIGO/VIRGO detector network (Abbott et al. 2016). If a BPASS binary system is still bound after both stars have undergone a SN and two compact objects have been created, the time until the merger is calculated using the GW radiation orbital energy-loss prescription from Peters (1964). The formation of a black hole or neutron star at the time of the SN is determined by the remaining bound mass after 10^{51} erg is injected in the star at the end of its life (Eldridge & Tout 2004). This remnant received a natal kick taken from a Maxwell–Boltzmann distribution with $\sigma = 265\,\mathrm{km\ s^{-1}}$ ((Hobbs et al. 2005) if the remnant mass is below $3\,M_{\odot}$, while the kick is reduced by a factor of $M_{\mathrm{remnant}}/1.4\,M_{\odot}$ above this limit.

For the prediction of the cosmic transient rates, we require the number of transients and the time from stellar birth to the transient for each of the BPASS stellar populations, which are 13 delay time distributions (DTDs), each at a different metallicity of which two are shown in Fig. 1 to show their dependence on metallicity. For example, the distribution of Type Ia SNe and compact object mergers differs between $Z = 0.020$ and $Z = 0.001$, while the PISNe and LGRBs are constraint to low metallicity populations (Heger et al. 2003, and references therein). But, as Fig. 1 shows, the total CCSN distribution is mostly unaffected by metallicity. It is, however, influenced by the presence of binaries, which increase the delay time of CCSNe to 250 Myr compared to the tens of Myr for single star evolution (Zapartas et al. 2017). These DTDs will be combined with the SFH to predict the transient rates.

3 STAR FORMATION ENVIRONMENT

3.1 Semi-analytical CSFR density

The CSFRD is fitted from empirically calibrated SFR indicators using UV and IR observations, which are sensitive to the assumed extinction from dust in distant galaxies (Wilkins et al. 2016, 2018). Early fits include a power-law time dependence (e.g. Behroozi et al. 2013), but more recent fits typically use a parametrization for redshift evolution introduced by Madau & Dickinson (2014):

$$\psi(z) = 0.001 \frac{(1+z)^{2.7}}{1+[(1+z)/2.9]^{5.6}}\ \mathrm{M_\odot\ yr^{-1}\ Mpc^{-3}}. \quad (1)$$

We transform equation (15) from Madau & Dickinson (2014) from a Salpeter (Salpeter 1955) to a Kroupa IMF by multiplying by 0.66, and this function is shown in Fig. 2 as the pink dashed line. It peaks at $z = 2$ while declining in the high and low redshift direction, with the current SFR being similar to $z \approx 6$. The CSFRD from Madau & Dickinson (2014) is widely used, as such it is our basis for comparison against simulations.

We combine the CSFRD with cosmic metallicity distribution and evolution from Langer & Norman (2006) as used in Eldridge et al. (2019) and Tang et al. (2020):

$$\Psi\left(\frac{Z}{Z_\odot}\right) = \frac{\hat{\Gamma}\left[0.84,\ (Z/Z_\odot)^2 10^{0.30z}\right]}{\Gamma(0.84)}, \quad (2)$$

where Γ and $\hat{\Gamma}$ are the complete and incomplete gamma functions, respectively, and Z is the volume-averaged metallicity of newly formed stars at redshift z.

We use the Aghanim et al. (2020) results as our cosmology throughout this paper ($h = 0.6766$, $\Omega_\mathrm{M} = 0.3111$, and $\Omega_\Lambda = 0.6889$). To be able to compare all the final rates, all SFHs have to be brought to the this cosmology. The empirical SFH extracted from UV observations has an h dependence coming from an $1/h^2$ for the SFR and a $1/h^3$ from the comoving volume. Since the Madau & Dickinson (2014) CSFRD is given in $\mathrm{M_\odot yr^{-1}Mpc^{-3}}$, we transform this by first reintroducing the h dependence followed by applying our cosmology. The SFHs from the cosmological simulations and cosmic event rate observations, on the other hand, have an h^3 dependence coming from the comoving volume, but similar to the empirical CSFRD we transform them to our cosmology.

3.2 Simulations

Observationally derived relations have the advantage of being data driven but are subject to uncertainties in observational completeness and model dependence in the calibrations required to recover the SFR or metallicity from the data. By contrast, cosmic volume hydrodynamic simulations represent a universe in which such effects are controlled, and the properties of stars are known precisely. However, they require a tremendous amount of computational power and are subject to their own uncertainties in the assumed physical interactions or subgrid prescriptions. These simulations start with dark matter and baryonic particles distributed through a simulation box according to initial conditions based on cosmic microwave background observations. The boxes are evolved up to the current time using simulated large-scale interactions, semi-analytical models for small-scale influences and in some cases also hydrodynamical gas modelling. The assumed strength of interactions and subgrid physics are tuned to match observations or according to theoretical prescriptions. To compare the impact of the SFH on transient rates, we compare the MilliMillennium, EAGLE, and IllustrisTNG simulations to cover different release years, sizes, and physical models.

3.2.1 *MilliMillennium Simulation*

The MilliMillennium Simulation is a subset of the *N*-body dark matter Millennium Simulation with ΛCDM cosmology with parameters $h = 0.73$, $\Omega_\mathrm{M} = 0.25$, and $\Omega_\Lambda = 0.75$ (Springel et al. 2005). Released in 2005, it contains 270^3 particles in a $62.5\,h^{-1}$ Mpc box, with each particle representing $8.6 \times 10^8\,h^{-1}\,\mathrm{M_\odot}$ dark matter with a special resolution of $5\,h^{-1}$ kpc. We will refer to the MilliMillennium as Millennium in this paper. As demonstrated by Stanway et al. (2018), this box is sufficiently large to recover the volume-averaged properties of the bulk galaxy population, although the full simulation would be required to recover rare systems such as extremely massive large scale structures. Starting at $z = 127$, 64 selected time-steps, known as snapshots, are stored with their gravitationally bound substructure subhaloes. These are identified by the SUBFIND algorithm Springel et al. (2001) and used to build a merger tree of subhaloes, which is the basic input for the semi-analytical models of galaxy formation (De Lucia & Blaizot 2007). When the gas surface density is higher than a critical value, star formation in a disk takes place and follows the parametrization by Croton et al. (2006); bulge star formation, however, only occurs during the merger of subhaloes and follows the Somerville, Primack & Faber (2001) collisional starburst model, which is only able to reproduce the observed gas fraction as a function of galaxy luminosity.

3.2.2 *EAGLE simulation*

Evolution and Assembly of GaLaxies and their Environments (EAGLE) (Crain et al. 2015; Schaye et al. 2015) is a hybrid *N*-body and hydrodynamical simulation. It contains dark matter particles with a mass of $9.70 \times 10^6\,\mathrm{M_\odot}$, and baryonic gas particles of $1.81 \times 10^6\,\mathrm{M_\odot}$ in a $100\,\mathrm{Mpc}^3$ box for the fiducial model (L0100N1504). The EAGLE simulation has a $\Omega_\mathrm{M} = 0.307$, $\Omega_\Lambda = 0.693$, and $h = 0.6777$ cosmology and does not provide their output with explicit dependence on the Hubble parameter. Therefore, we use the simulations cosmology to reintroduce the h^3 dependence and then apply our cosmology to allow for comparison. While only 29 snapshots were recorded between $z = 127$ and $z = 0$, 1504^3 particles were used to study galaxy formation. The stellar formation is resolved using subgrid physics and depends on the pressure in dense gas, and is tuned to reproduce the observed Kennicutt–Schmidt relation (Schmidt 1959). The simulation includes prescriptions for black hole and SN feedback mechanisms that return baryons to the intergalactic medium and enrich the environment. A full description can be found in Wiersma et al. (2009). The feedback mechanisms and star formation rate (SFR) are calibrated to reproduce the galaxy luminosity function at $z = 0.1$, BH–stellar mass relation, and galaxy size (Crain et al. 2015). A merger tree is constructed using the same SUBFIND algorithm as the Millennium simulation, but with slight adjustments and inclusion of baryonic matter in substructure identification (Dolag et al. 2009).

3.2.3 *IllustrisTNG simulation*

Similar to EAGLE, The Next Generation Illustris simulation (IllustrisTNG) is a hybrid simulation that contains dark matter and baryonic matter. These have particle masses $7.5 \times 10^6\,\mathrm{M_\odot}$ and $1.4 \times 10^6\,\mathrm{M_\odot}$, respectively, in the TNG100-1 simulation (Marinacci et al. 2018; Naiman et al. 2018; Nelson et al. 2018; Springel et al.

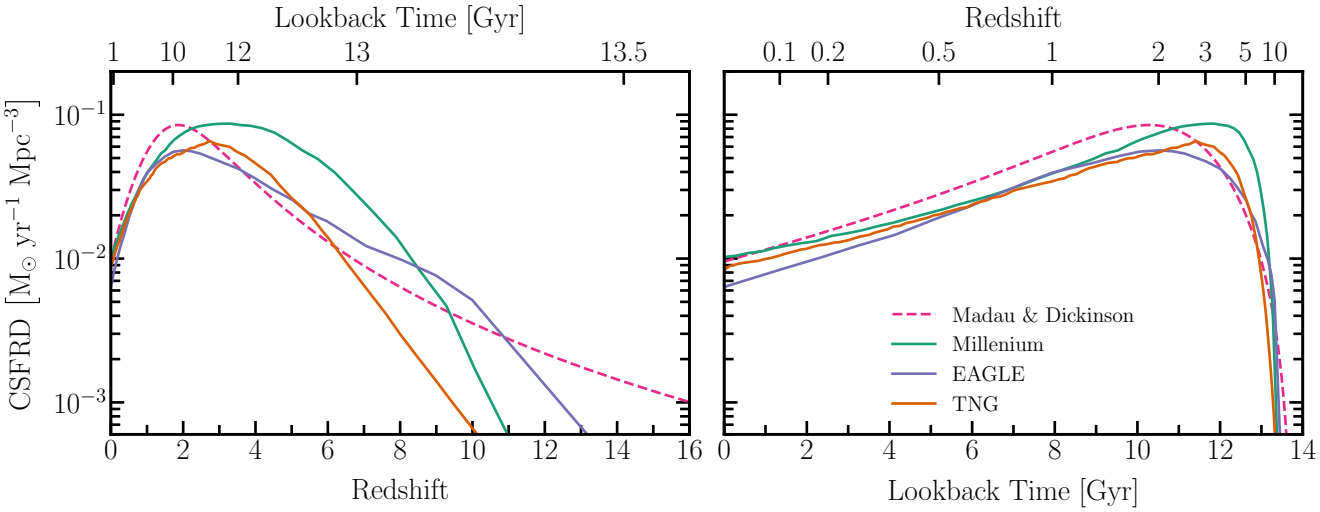

Figure 2. The CSFRD over redshift (left) and lookback time (right) for the empirical prescription from Madau & Dickinson (pink dashed), and rates extracted from the Millennium (green), EAGLE (purple), and IllustrisTNG (orange) simulations.

2018; Pillepich et al. 2018b), which we shall refer to as the TNG simulation in this paper. 1820^3 dark matter and 1820^3 baryonic particles are included in the simulation volume of 110.7^3 cMpc and are evolved from $z = 127$ to present day in a $h = 0.6774$, $\Omega_M = 0.30897$, and $\Omega_\Lambda = 0.6911$ ΛCDM universe from Ade et al. (2015). Again, we scale to our own cosmology. Like the other two simulations, the IllustrisTNG is a hydrodynamic simulation but also includes magnetic fields and new feedback prescriptions. These and the galaxy formation models are fully described in Weinberger et al. (2017) and Pillepich et al. (2018a) and aim to agree with observational constraints, such as the CSFRD and the stellar mass content of galaxies at $z = 0$. Again, the SUBFIND algorithm finds subhaloes (galaxies), but the IllustrisTNG introduces a 'SubhaloFlag' to identify gravitationally bound clusters that are numerical artefacts and not of cosmological origin (Nelson et al. 2019). We remove non-cosmological subhaloes from our sample. By tracing the baryonic content of each galaxy, the SUBLINK algorithm generates merger trees (Rodriguez-Gomez et al. 2015).

4 NUMERICAL METHOD

For the cosmological simulations, we extract the merger trees of each non-zero stellar-mass galaxy at $z = 0$ using the public APIs [EAGLE (McAlpine et al. 2016), TNG (Nelson et al. 2018), Millennium (Lemson & Consortium 2006)]. Each galaxy has its own individual metallicity and SFR evolution influenced by stellar evolution and galaxy interactions, allowing for a broader range of galaxy metallicities than the empirical CSFRD. The SFR distribution over metallicity and redshift in Fig. 3 shows that the cosmological simulations have a wider metallicity spread and faster enrichment of the universe than the empirical parametrization. The latter is especially true for the Millennium simulation, which achieves a mean metallicity of 0.004 at $z = 10$ and stays nearly flat throughout cosmic history, only increasing to 0.01 at $z = 0$. This is similar to the mean metallicity evolution of the TNG simulation, which remains mostly flat with only a fast increase between $\log_{10}(1 + z) = 0.8$ and $\log_{10}(1 + z) = 1.0$. The EAGLE and empirical distributions, on the other hand, have a gradual increase in their mean metallicity towards current time. In the case of the EAGLE, we even see evidence for a bimodal distribution in the metallicity evolution with a constant high metallicity population at $Z = 0.015$ from $\log_{10}(1 + z) = 0.8$ to current time, and a second lower metallicity population that is present from the start of star formation and slowly increases in metallicity over redshift. This complex behaviour cannot be reproduced in the analytical models typically used. This, for example, allows for low metallicity events to still occur when high metallicity events are more prevalent.

Using the metallicity and star formation at each snapshot for each galaxy and the dimensions of the simulation, we construct a volume-averaged CSFRD, as shown in Fig. 2. At redshifts below $z = 2$, the shapes of the CSFRDs are similar but differ in normalization with the Millennium CSFRD and semi-analytical prescription having the highest SFRs at $z = 0$ followed closely by the TNG and EAGLE CSFRD. The $z = 0$ and $z = 2$ SFR rates are shown in Table 1. Above $z = 2$, the shape of the Millennium CSFRD and the long tail of the empirical CSFRD stand out. It is significantly different than the other CSFRD by peaking later with a broader spread at $z = 3.31$. The empirical CSFRD, on the other hand peaks sharply at $z = 1.87$ with the tail continuing into high redshift, while the rates of the cosmological simulations at these early times, when we expect low metallicity to dominate, are low to non-existent.

Based on the mean stellar metallicity reported by the simulation, individual galaxies are binned into one of the 13 BPASS metallicities, resulting in metallicity-specific SFR over redshift, as shown in Fig. 4. The empirical CSFRD from (Madau & Dickinson 2014) is split into the same metallicity bins using the prescription from Langer & Norman (2006), as described in Section 3.1. The metallicity distributions in Fig. 4 indicate an early start in high metallicity star formation in the cosmological simulations. At $z \sim 6$ solar metallicity star formation is ongoing, while the empirical prescription only starts formation at this metallicity at $z = 4$. The faster enrichment significantly impacts the rate of specific transients due to their sensitivity to metallicity, see Section 2. Furthermore, a late start in star formation in the cosmological CSFRD reduces the amount of low-metallicity star formation at high redshift.

To estimate transient rates, the metallicity specific SFHs have to be combined with the associated transient DTDs from Section 2. This is achieved by splitting the final lookback time into equal-sized bins

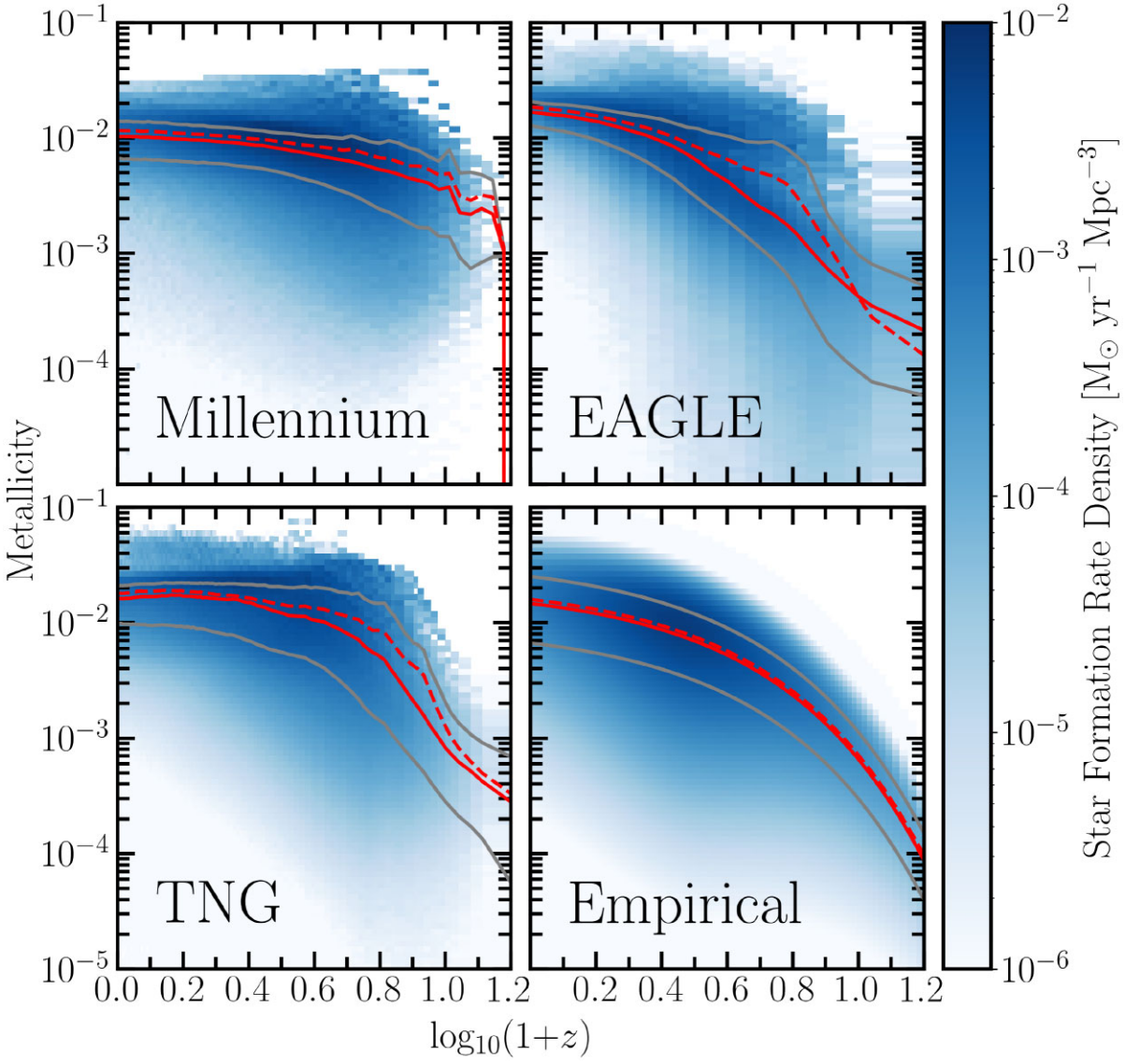

Figure 3. The SFR density distribution over metallicity and over $\log_{10}(1+z)$. The median SFR weighted metallicity is indicated with the red solid line with the 1σ spread shown by the solid grey lines. The dashed red line indicates the SFR weighted mean metallicity. The empirical prescription has a slow increase over redshift, while the Millennium simulation has the opposite evolution with a near flat high median metallicity over redshift. The EAGLE and TNG start at low metallicity at high redshift and have a fast increasing metallicity as the universe evolves to current day.

in linear space. For each bin (j) we calculate the rate (R) as described in equation 3, where t_i are the bin edges. We integrate the SFH using linear interpolation to account for changes between snapshots. The integrated DTD and SFH are multiplied, summed over each time bin, and the result is divided by the bin width, resulting in the number of events per year per Gpc.

$$R_j = \frac{\sum_{i=j+1}^{N} \int_{t_{i-1}}^{t_i} \mathrm{SFH} \int_{t_i - t_{j+1}}^{t_i - t_j} \mathrm{DTD}}{(t_{j+1} - t_j)}. \quad (3)$$

The described method has been made available as a module in HOKI, which is a python framework and interface for BPASS models (Stevance, Eldridge & Stanway 2020). The CSP module contains several built-in stellar formation histories and allows the user to input their own binned or parametrized SFH to generate complex stellar populations. Moreover, it calculates BPASS transient rates originating from this population at a specific lookback time or over the complete history of the universe.

5 ESTIMATED TRANSIENT RATES

5.1 Type Ia Supernovae

The formation of a white dwarf and subsequent accretion or merger leading to a thermonuclear explosion takes at least 10^8 years in BPASS depending on metallicity and stellar evolution, due to the inherent binary nature of this event. With the long time between stellar birth and SN, the Type Ia rate probes older star formation (Ruiter, Belczynski & Fryer 2009; Mennekens et al. 2010; Ruiter et al. 2011; Maoz & Mannucci 2012; Eldridge et al. 2019), which we confirm by comparing the peaks of star formation against the peaks

Table 1. The cosmic event rate predictions, $\log(\mathcal{R})$, at $z = 0$ in a events per year per Gpc^3 for the different SFHs. CCSN contain the Type II, IIP, Ib, and Ic SNe types. The SFRs at $z = 0$ and $z = 1$ are shown for comparison against the rates.

	Empirical	Millennium	EAGLE	TNG
		$\log_{10}(\mathcal{R})$ (yr^{-1} Gpc^{-3})		
BBH	2.01	2.01	1.70	1.63
BHNS	2.38	2.36	2.03	2.04
BNS	2.35	2.33	2.16	2.23
Ia	4.25	4.22	4.06	4.12
LGRB	2.29	2.04	1.13	1.55
PISN	0.82	0.71	−0.09	0.10
CCSN	4.92	4.96	4.74	4.86
II	4.20	4.27	3.84	4.03
IIP	4.64	4.69	4.45	4.58
Ib	4.15	4.13	4.07	4.17
Ic	3.98	4.04	3.88	3.99
		$\log_{10}$(SFR) ($M_\odot$ yr^{-1} Mpc^{-3})		
SFR $z = 0$	−2.02	−1.99	−2.20	−2.08
SFR $z = 2$	−1.08	−1.13	−1.25	−1.26

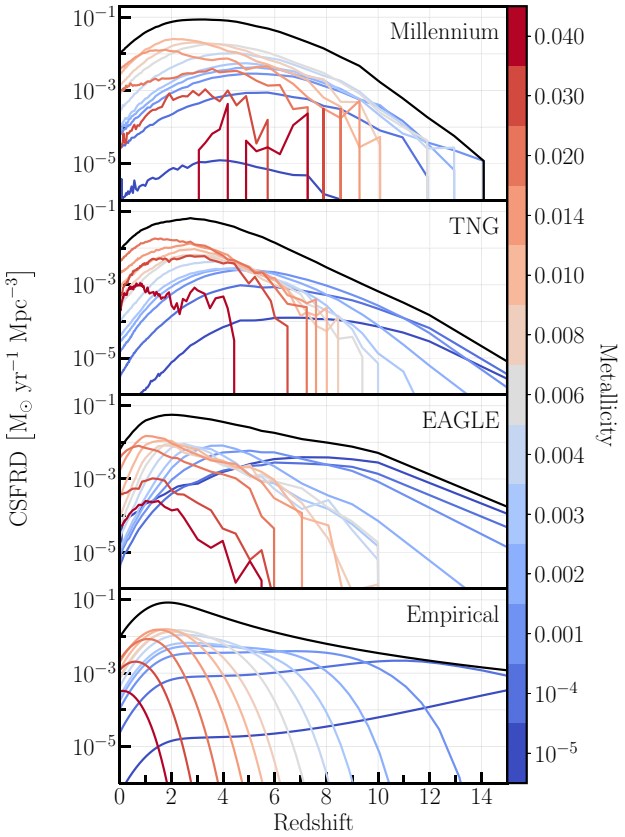

Figure 4. The CSFRD for our empirical prescription, and the Millennium, EAGLE, and TNG simulations split into the 13 BPASS metallicity bins indicated by the colour bar. The total SFR density is indicated by the black solid line.

of the Type Ia rate in Table 2. The peak Type Ia SN rate occurs $\Delta(z) \approx 1-2$ later than the peak in star formation with the exact delay depending on the simulation and its metallicity evolution.

The rates over redshift are shown in Fig. 5 together with a collection of observations, which are summarized in Table A1. The

Table 2. The redshift (z) of the peak in SFH, Type Ia, CCSN, PISN, and BBH rates.

	SFH	Type Ia	CCSN	PISN	BBH
			Redshift (z)		
Empirical	1.87	0.98	1.87	2.63	1.90
Millennium	3.31	1.21	3.31	4.40	2.78
EAGLE	2.01	1.17	2.01	5.87	2.27
TNG	2.73	1.09	2.73	4.40	2.63

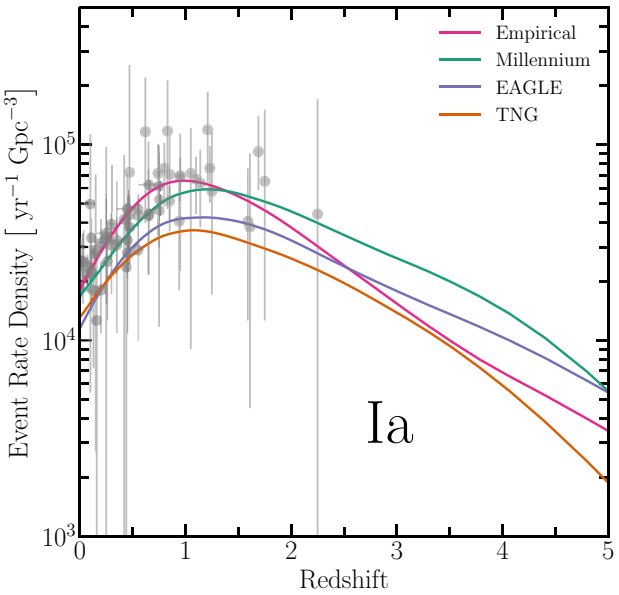

Figure 5. Type Ia SN rate predicted from the four stellar formation histories, compared with observations drawn from a collection of surveys described in Table A1.

Table 3. The reduced χ^2 value from each model using the given data, where N is the number of observed cosmic event rates for the specific event type.

Transient	N	Empirical	Millennium	EAGLE	TNG
Type Ia	60	0.32	0.28	0.81	0.95
CCSN	25	1.25	1.01	0.62	0.58
PISN[a]	5	0.38	0.84	0.61	1.17
All	90	0.58	0.51	0.74	0.86
LGRB*	10	1.82	3.53	4.67	7.13

Note. All weights each observed rate equally. Asterisk ($\star$) includes the tidal LGRB contribution from Chrimes et al. (2020) and is, therefore, left out of the All. [a]The calculated rate from Zhao, Xue & Cao (2020) is left out due to the absence of an uncertainty on the observation.

Millennium and empirical predictions lie around these observations, while the EAGLE and TNG simulations underpredict the rates and only align with a few observed rates at $z < 0.5$. The accurate empirical prediction is in contrast to the overestimation in Eldridge et al. (2019) due to reweighing of the CSFRD from a Salpeter to a Kroupa IMF. The model predictions, however, differ less than a factor of 2. To assess the goodness of the predictions, we calculate the reduced χ^2 and see in Table 3 that the EAGLE and TNG has reduced χ^2 closest to 1. However, we note that due to the large uncertainties of the observations, all reduced χ^2 of the Type Ia predictions are below 1, indicating that the choice between these SFH and metallicity

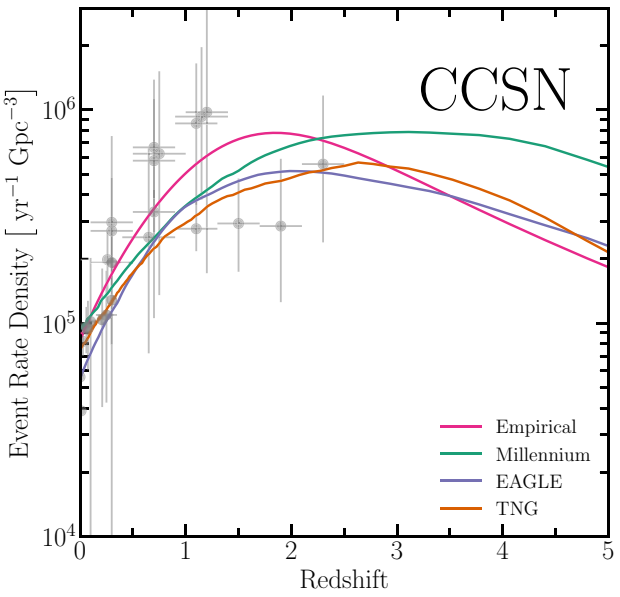

Figure 6. Predicted CCSN rates with a compilation of observational estimates in grey for comparison (see Table A2).

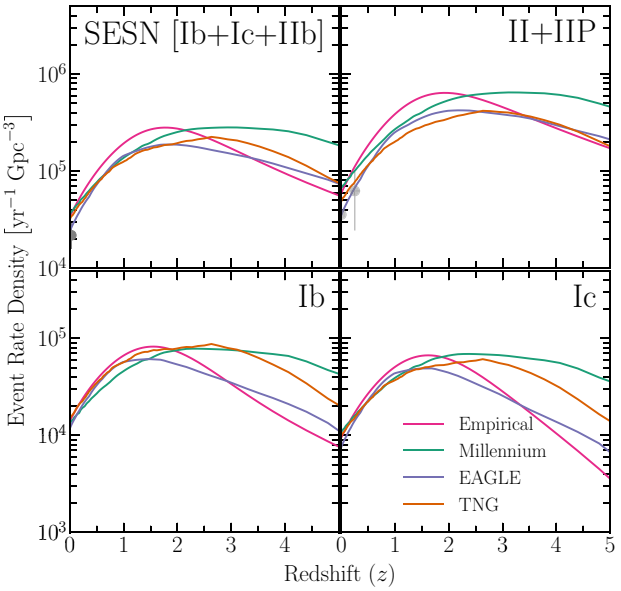

Figure 7. The CCSN events split up by possible subtypes with a single observed stripped-envelope SN (SESN) rate by Frohmaier et al. (2021), and two Type II observations (see Table A4).

evolution are minimally important in predicting the Type Ia rate given current observations.

5.2 Core-collapse supernovae

CCSNe occur in young stellar populations, because the CCSN progenitors are massive stars that burn through their nuclear fuel quickly and, thus, have short delay times ($10^{6.5}$–$10^{8.3}$ yr). This creates a tight relationship between the SFR and cosmic CCSN rate, as the alignment of the peaks between the CCSN rate and SFH peaks in Table 2 shows. Not only do the peaks align, the CCSN predictions over redshift also closely track the shape of the associated CSFRD, and are shown in Fig. 6 with observations from Table A2. Below $z = 0.5$, they follow observations closely till around $z = 0.9$ after which the observations are split in two clusters. The first has data points around $z = 1$ and $z = 1.5$ with high CCSN rates originating from a collection of surveys (Graur et al. 2011; Dahlen et al. 2012; Melinder et al. 2012). At these redshifts, the empirical CCSN rate prediction has the best-fitting rates. The cosmological CCSN rate predictions align better with the second cluster of data points, which are located between $z \sim 1$ and 2.5, have lower rates, and originate from a single survey by Strolger et al. (2015). Different approaches in correcting for missed SNe due to high extinction could result in this grouping. Because the CCSN rate follows star formation closely, they often happen in very dusty star forming regions and can be obscured, especially at high redshifts. Hence, the fraction of missed SNe has to be accounted for. The higher estimates use a prescription from Mattila et al. (2012), which can increase the CCSNe rate significantly. Local overdensities of star formation in the survey fields might also cause these observations to be overestimated (Dahlen et al. 2012). Strolger et al. (2015), on the other hand, use their own method based on the Calzetti et al. (2000) extinction law, but these high redshift observations are challenging and only survey a small area compared to other SN surveys leaving them more vulnerable to cosmic variance and low number counts. Finally, this grouping and the large standard deviation of the first cluster results in a 1.01 reduced χ^2 for the Millennium simulation and slightly worse values for the empirical, EAGLE, and TNG predictions as shown in Table 3.

5.2.1 *CCSN subtypes*

Although the same explosion mechanism causes CCSNe, the subtypes come from progenitors with different mass ranges and mass-loss histories, as described in Section 1. By looking at the rate of the subtypes and their fraction to the total CCSN rate, we extract more information about the progenitors. However, the limited number of SESN events restricts the calculation of an observed rate. Frohmaier et al. (2021) is one of the few studies to calculate the total combined rate for Type IIb, Ib, and Ic events. Since BPASS does not distinguish between Type II subtypes except for Type IIP events, we use the fraction from Eldridge et al. (2013) of 0.6541 to estimate the Type IIb rate from the non-IIP Type II events. This fraction is not well constrained and differs for other surveys (e.g. Smith et al. 2011; Li et al. 2011a). Fig. 7 shows that the predicted rates lie above the Frohmaier et al. (2021) observed rate estimate of 2.18×10^4 yr^{-1} Gpc^{-3} in our cosmology at $\langle z \rangle = 0.028$. Rates calculated using the EAGLE model approaches this rate with 2.40×10^4 yr^{-1} Gpc^{-3}, but the other SFHs overpredict the observed rate with the Millennium Simulation deviating the most with a rate of 3.65×10^4 yr^{-1} Gpc^{-3}.

The Type II rate predictions align with observed rates from Li et al. (2011b) and Cappellaro et al. (2015) in Table A4, although the empirical and Millennium SFHs result in an overestimation of this subtype. For the other CCSN subtypes, Type Ib and Type Ic, no observational cosmic rates are available for comparison. Instead, we note that the Type Ib and Ic rates have similar shapes due to similar progenitors and sensitivity to the metallicity evolution. The absolute rate of Type Ib events, however, is slightly higher than Type Ic due to the difficulty of stripping the helium envelope required for a Type Ic SN. Distinguishing between the individual predictions for either of these SN types is impossible at low redshift due to the minimal difference in the rates, which could be attributed to a small difference

Table 4. Fraction of CCSN subtypes at $z = 0$ for predicted rates. Shivvers et al. (2017) is volume-limited to 60 Mpc. Due to rounding, the empirical fractions do not add up to 1.

	II (IIP & non-IIP)	Ib	Ic
		CCSN fraction	
Empirical	0.71	0.17	0.11
Millennium	0.73	0.15	0.12
EAGLE	0.64	0.22	0.14
TNG	0.67	0.20	0.13
Shivvers et al. (2017)	0.80	0.11	0.09

in metallicity between the predictions. The metallicity distributions in Fig. 3 shows that the EAGLE, TNG and empirical CSFRDs have similar metallicities at these low redshifts, while the Millennium simulation has a slightly lower mean metallicity. However, above a metallicity of half solar, the Ib/c rates in the DTD are near constant, which, together with the similar CSFRD, results in similar rates for the cosmic Type Ib/c predictions. At higher redshifts, the metallicity and CSFRDs become more distinct, which separates the cosmic Type Ib/c rates, as can be seen in Figs 2 and 7. The Type II SN rates are an order of magnitude higher than the Type Ib and Ic rates and dominate the CCSN predictions, because the progenitor systems do not need to undergo envelope stripping and can be of single or binary star nature, resulting in the predicted rates more closely following the CSFRD.

5.2.2 *CCSN subtype fraction evolution*

While the cosmic rates of CCSN subtypes are hard to come by, the fractions of Ib, Ic, and IIb with respect to the total number CCSNe are available from several surveys (Smith et al. 2011; Li et al. 2011a; Shivvers et al. 2017; Perley et al. 2020). Therefore, we show our predictions and the fractions from the volume-limited survey up to 60 Mpc from Shivvers et al. (2017) in Table 4. Our Type II predictions are significantly lower than the observed fraction. The magnitude-limited survey from Perley et al. (2020), however, predicts a lower Type II fraction of 0.722, which is closer to our predictions, although still significantly higher than the 0.64 and 0.67 fractions for the EAGLE and TNG predicted fractions. A slightly higher fraction of 0.766 is found by the 100 Mpc volume-limited survey by Smith et al. (2020). Instead of the Type II events, there are fractionally more Type Ib/c events in our predictions of which the bulk are Type Ib events. This discrepancy could indicate too swift an enrichment, a too strong stellar wind prescription, a different mass transfer efficiency, or a combination of the above. Since the EAGLE and TNG simulations enrich faster than the Millennium simulation and empirical description, this is the likely origin.

Looking at the evolution of the relative fractions of SNe that originate from massive stars in Fig. 8 makes it clear that the Type IIP remains constant over redshift, because these typically come from single stars and wide binaries. In comparison, the other type II SN fraction decreases with decreasing redshift, being replaced by Type Ib/c. The reason for this is that while binary interactions remove much of the envelope, stellar winds play a significant role in the further evolution. Thus, more metal-rich stellar populations are dominated by SNe that have experienced more mass loss. The scale of this change depends on the metallicity distribution as shown in Fig. 3, where the mean metallicity evolution of the Millennium simulation is near flat, as is the evolution of the Type Ib/c rate in Fig. 8. The other SFHs, on the other hand, have a clear metallicity evolution, which shows in the relative fraction change indicating that the Type Ib/c fractions over redshift are good tracers for the metallicity evolution, and might allow future observations of these rates to constraint the IMF and cosmic metallicity evolution, albeit model uncertainty (Fryer et al. 2021).

5.3 Long gamma-ray bursts

LGRB afterglows have been observed as coincident with broad-lined Type Ic (Ic-BL) and represent a subset of energetic Ic events, where a relativistic jet is launched from the surface of a nascent black hole or magnetar formed during core-collapse (e.g. Heger et al. 2003; Langer 2012). The furthest GRB has been measured at $z = 9.4$ (Cucchiara et al. 2011), but it is difficult to derive a volumetric rate for such sources because their emission is highly relativistic beamed. As a result, their observability depends on the event's geometry, specifically the jet opening angle.

We use the observed GRB rate over redshift from the SHOALS sample (Perley et al. 2016) that we correct for the event geometry and missed low-luminosity events. To achieve this, we adopt the method from Chrimes et al. (2020), and integrate over the GRB luminosity function of Pescalli et al. (2016) from a isotropic equivalent energy of $E_{\rm low} = 10^{48.1}$ erg to $E_{\rm max} = 10^{56}$ erg, while correcting for an opening angle of $\theta = 9.9^{\circ}$. The grey triangle in Fig. 9 shows the corrected SHOALS rate.

The predicted LGRB rates from BPASS, shown as solid lines in Fig. 9, only contain events formed through chemically homogeneous evolution at low metallicities (Eldridge et al. 2017), which is lower than observed, as expected. Additional tidal formation pathways have been added post-process by Chrimes et al. (2020, dashed line in Fig. 9). These pathways mostly contribute at low redshifts and boost the predicted rate to a similar order of magnitude as the observations. However, the shape of the predicted rates no longer follows the same gradient as the observations and peaks at lower redshift. Due to the difficulty in constraining the observed rate and because the agreement is, of course, in part a consequence of the tuning of the LGRB opening angle parameters with a similar empirical CSFRD prescription as adopted here (Chrimes et al. 2020), it is not possible to distinguish between the SFHs as of yet.

Although the LGRB are related to the Type Ic, their relative fractions evolve in opposite fashion in Fig. 8. While the Type Ic increase over redshift, the LGRB rate drops significantly, because angular momentum required for the LGRB is removed by the stronger stellar winds in a more enriched universe (Vink et al. 2001; Woosley et al. 2002) and are therefore sensitive to low metallicity star formation. This relation between the two event rates can help us probe the metallicity distribution of a stellar population, especially since the chemically homogeneous LGRB event have a short delay allowing us to probe the change in low metallicity star formation.

5.4 Pair instability supernovae

Very massive stars ($\gtrsim$100 $M_{\odot}$) reach the end of their life in only a few million years. The fast fusion leads to a low internal core density, while the temperature in the helium core reaches electron–positron production levels, causing the radiative pressure to drop due to the removal of photons. Without a force to counteract gravity, the star collapses in a PISN and completely disrupts the star, leaving no remnant behind (Fowler & Hoyle 1964; Rakavy & Shaviv 1967; Heger & Woosley 2002). The short lifetime, due to the high hydrogen burning rate, and the high-metallicity sensitivity makes this event a

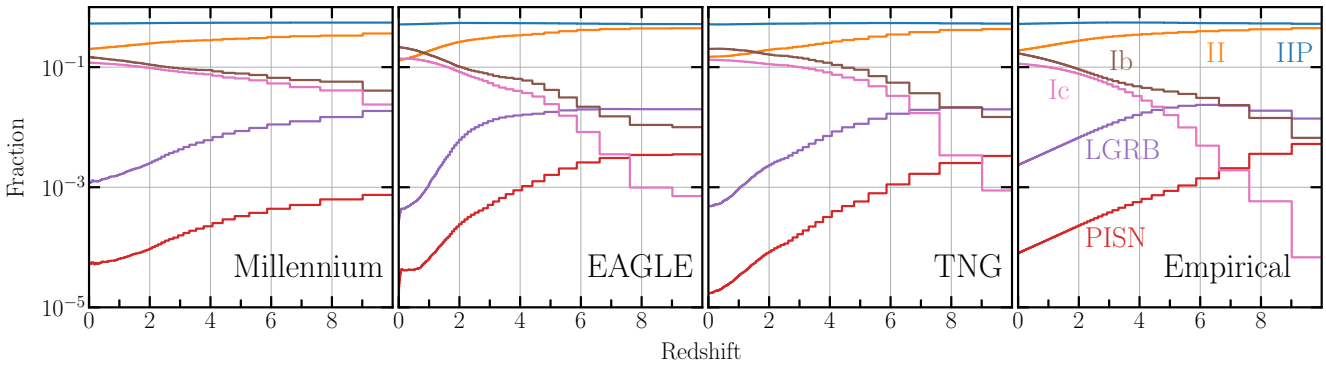

Figure 8. The relative fraction of all SNe that originate from massive stars for each of the considered environment prescriptions. LGRB, PISN, and Type II rates (purple, red, orange) decrease as the universe enriches, while the Type Ib/c (brown and pink) rates increase. The fraction of massive stars ending their life in a Type IIP SN (blue) is near constant over redshift.

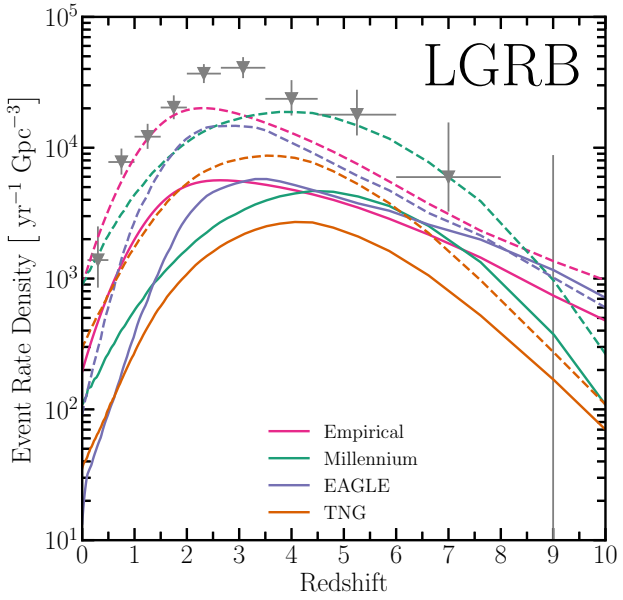

Figure 9. The predicted LGRB rates from the standard BPASS output (solid) with additional post-processed LGRB tidal pathways added from Chrimes et al. (2020) (dashed) are shown for all four environment prescriptions. The opening angle and luminosity corrected SHOALS rates are shown for comparison (grey triangles) (Perley et al. 2016).

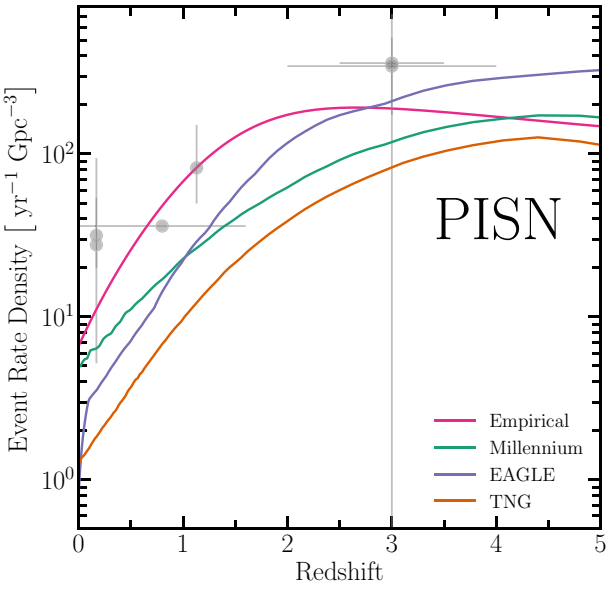

Figure 10. Predicted PISN rates with observational rates from SLSN-I measurements (see Table A3).

perfect candidate for SFH probes (Fryer, Woosley & Heger 2001; Yusof et al. 2010, 2013; Dessart et al. 2012; Eldridge et al. 2019).

Currently, no smoking-gun evidence of a PISN has been observed, although a few hydrogen-poor SLSN-I have been identified as possible candidates (Woosley et al. 2007; Gal-Yam et al. 2009; Cooke et al. 2012; Terreran et al. 2017; Gomez et al. 2019). Their energy requirements are too high to be consistent with the classical core-collapse mechanism, but this remains unproven (Kozyreva & Blinnikov 2015) and alternative explanations, such as magnetars (Howell 2017; Kasen & Bildsten 2010; Woosley 2010; Inserra et al. 2013), rotational PISN (Renzo et al. 2020), and late leakage from pulsar wind nebula (Dessart et al. 2012), are also likely. None the less, in Fig. 10 we have used the observed rate of SLSN-I that are possible PISN, which are summarized in Table A3, for comparison. The event rates from the simulations show the non-smooth nature of the low metallicity SFR at low redshift, specifically the EAGLE simulation. Its event rate has a significant drop at $z = 0.1$ which is caused by a drop in the low-metallicity star formation. Since they have limited star formation at low redshift and PISN mostly occur in low metallicity environments, only the predicted event rate from the empirical CSFRD aligns with the observations. The uncertainty in the formation pathway of SLSN-I makes it not possible to state if SLSN-I are a good indicator for the PISN rate, except that their observed rate is within an order of magnitude of our predictions.

5.5 Compact objects

5.5.1 Binary black-hole mergers

The binary nature of compact object mergers leads to the domination of events with delay times of at least $10^{6.5}$ yr, which would result in the peak of BBH mergers occurring after the peak SFH. However, since the BBH merger rate is sensitive to metallicity and mostly occurs at low metallicity, this does not have to be the case. As we see in Table 2 and in Fig. 11, only the TNG and Millennium predictions have their peak at a lower redshift than their maximum SFR, while the

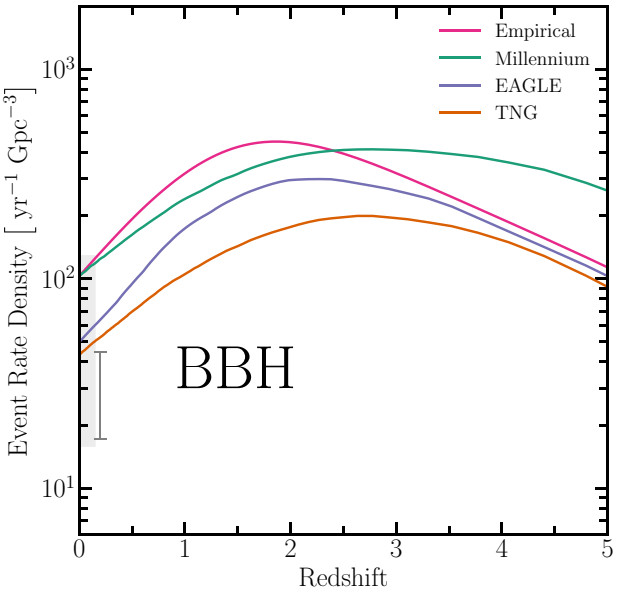

Figure 11. BBH merger rate predictions with observations from Abbott et al. (2021a) with the lowest 5 per cent to highest 95 per cent credible interval of their considered population models at $z = 0$ and $z = 0.2$ for the non-evolving and evolving merger rates, respectively. The $z = 0$ rates are shaded and extended out to $z = 0.15$ for clarity.

empirical and EAGLE predicted BBH rates peak at a higher redshift than their peak SFR. This indicates that most of the BBH events originate from low-metallicity populations in the earlier universe as expected.

A more direct comparison is possible with recent results from GWTC-3, which includes estimates for a variety of population models at $z = 0$ for non-evolving merger rates and at $z = 0.2$ for redshift-dependent rates (Abbott et al. 2021a). Fig. 11 shows their range when only considering the lowest 5 per cent and highest 95 per cent credible boundaries out of the `PDB (ind)`, `MS`, and `BGP` models (For a description of the models see Abbott et al. 2021a), whose ranges are shown in Fig. 12. All predictions fall within the combined 90 per cent credible interval from 16 to 129 yr^{-1} Gpc^{-3} for the non-evolving merger rate at $z = 0$, although the Millennium and Empirical predictions are at the higher end of the observational range. However, the merger rate increases over redshift and when this is taken into consideration the observed rate decreases to 17.1–45 yr^{-1} Gpc^{-3}, as the bar at $z = 0.2$ in Fig. 11 shows. This combined credible interval has been constructed in similar fashion to that at $z = 0$, but considers three BBH population models: `PP`, `FN`, and `PS` (For a description of the models see Abbott et al. 2021a), which evolve over redshift. At $z = 0.2$, the observational constraints from Abbott et al. (2021a) are the strongest and the combined 90 per cent credible range from their collection of models lies below the predicted merger rates, despite that the simulations with a fast enrichment, the EAGLE and TNG simulations, approach upon this range, which shows the strong correlation between the BBH rate and metallicity evolution.

More detail can be obtained by looking at the specific population models used by Abbott et al. (2021a) instead of looking at the combined credible interval. The conversion from measured to intrinsic rates introduces several model-dependent uncertainties in the BBH rate and can move the observed rate both towards and away from our predictions. For the constant merger rate at $z = 0$, shown in the left-most panel in Fig. 12, the majority of uncertainty in the credible interval comes from the `Mixed-Source model`, while the other models are clustered around the same rate of ∼30. The predicted rates from the empirical prescription and Millennium simulation are an order of magnitude higher than these observed rates. Only the TNG and EAGLE simulation are close to this range, but still overestimate the predicted BBH merger rate compared to the `PDB (ind) model` by a factor of 2.0 and 2.2, respectively. The fact that the TNG simulation also overestimates the fiducial evolving observed rate (`PP`) by 1.9, indicates a systematic overprediction. This might be an effect of the details of the assumed populations compared to `BPASS`, where more low-mass black holes are formed (Ghodla et al. 2021), thus resulting in our predicted rates for BBH mergers being too high.

On the other hand, Abbott et al. (2021a) also found that the BBH rate increases with a factor of $2.7^{+1.8}_{-1.9}$ between $z = 0$ and $z = 1$, which lies between the predicted values from the Millennium (2.3), TNG (2.4), empirical (3.1), and EAGLE (3.5) predictions, indicating that the rate only requires a small downward adjustment to within the observed range that can be achieved by the following methods:

First, the BBH merger rate is sensitive to the environmental parameters, such as the SFR and metallicity evolution in the early universe (Dominik et al. 2013; Mapelli et al. 2017, 2019; Lamberts et al. 2018; Neijssel et al. 2019; Santoliquido et al. 2020a; Artale et al. 2020; Tang et al. 2020), where the differences between SFH in our simulations are most apparent. This effect shows in the predicted rates with the TNG and EAGLE simulation having a faster enrichment and lower BBH rates. An even faster increase in mean metallicity could reduce the BBH cosmic rate further, but this would also increase the overpredicted Type Ib/c fraction and further underestimate the LGRB rate. Although the constraints on the observed fraction and LGRB rate are limited, we should also focus on other influences on the cosmic BBH merger rate, such as the assumed constant binary fraction over redshift and metallicity. For close binary systems with solar-type stars, the binary fraction decreases significantly with metallicity (Moe, Kratter & Badenes 2019). A similar relation might hold for massive stars, but the binary fraction is difficult to infer from early Universe observations.

The second area of interest is the physics and parameters assumed in the stellar evolution models. While the BNS merger rate is most sensitive to these parameters (Broekgaarden et al. 2021a), specific processes could contribute to a lower BBH rate but unchanged BNS rate. For example, altering the prescription used to predict SN outcomes (Dabrowny, Giacobbo & Gerosa 2021), including pulsation pair-instability (Belczynski et al. 2016; Farmer et al. 2019; Stevenson et al. 2019; du Buisson et al. 2020), or increasing the stellar winds at low metallicities (Mapelli 2021, and references therein) can decrease the compact remnant masses, making it easier for systems to become unbound, thus, possibility reducing the BBH and BHNS rate. In the case of the latter, the pulsation pair-instability can even prevent black holes from forming within the pulsation pair-instability mass gap. However, untangling the effect and strength of each component of the assumed physics of the natal kick (du Buisson et al. 2020; Igoshev et al. 2021), mass transfer efficiency, and common envelope prescription (van Son et al. 2020; Klencki et al. 2021; Marchant et al. 2021; Bavera et al. 2021b) on the resulting BBH, BHNS, and BNS rates is non-trivial and an active area of research (Santoliquido et al. 2020a; Olejak, Belczynski & Ivanova 2021; Broekgaarden et al. 2021a).

Finally, including GW190814 in the BBH merger rate can drastically change the observed intrinsic rate. For example, in Abbott et al. (2020) the inclusion of GW190814 changes the observed rate to 57^{+52}_{-29} Gpc^{-3} yr^{-1} in the cosmology used in this paper, due to an increase in the expected number of low-mass black holes resulting in

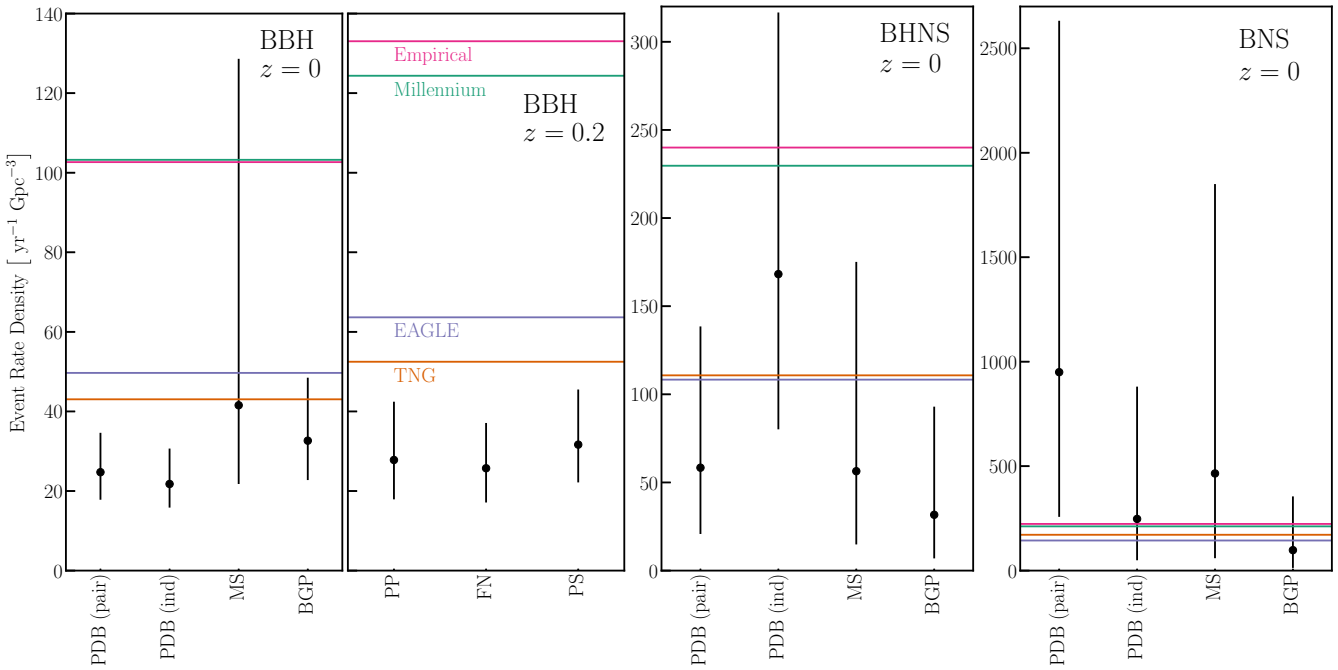

Figure 12. Observed BBH, BHNS, BNS merger rates from different assumed population models by Abbott et al. (2021a) as black circles with their 90 per cent credible interval marked. At $z = 0$, these population models assume a non-evolving BBH rate, while the $z = 0.2$ observed rates do assume an evolving merger rate over redshift. The predicted rates, which evolve over redshift, are sampled at the relevant redshift to compare against the observed rates.

nearly the same rate as predicted by the EAGLE and TNG simulations at $z = 0$. The nature of GW190814, however, is an area of active discussion and the models by Abbott et al. (2020) do not extrapolate well to the GW190814 masses ($M < 3M_{\odot}$).

5.5.2 *BNS mergers*

Like the BBH population, the BNS rate has been directly measured at $z = 0$ using GW measurements. While short gamma-ray burst can provide observations at higher redshift, the conversion from measurement to intrinsic rate suffers from a similar dependence on opening angle as LGRB. The intrinsic merger rate is mostly independent of metallicity (Giacobbo & Mapelli 2018; Tang et al. 2020), but is highly sensitive to the natal kick and Common Envelope Evolution prescription (Dominik et al. 2013; Chruslinska et al. 2018; Giacobbo & Mapelli 2018; Santoliquido et al. 2020a). Fig. 13 shows that all four predictions lie within the maximum credible region at $z = 0$, which is a positive sign for the implemented physics model. Breaking down the measured interval further in Fig. 12, we see that the rates fall within the boundaries of most populations models considered by Abbott et al. (2021a), expect for the `PDB (pair) model`, which has a higher BNS merger rate than any of the models predict. Our predictions agree with the other population models, but no environmental prescription is preferred by the BNS rate, which is as expected since it is mostly independent of environmental parameters. Instead, better constraints can be placed by looking at the BNS chirp mass distribution and surviving BNS systems, however such comparisons go beyond the scope of this paper.

5.5.3 *Black hole–neutron star mergers*

After observations from Abbott et al. (2021b) produced a weak constraint on the BHNS merger rate, Abbott et al. (2021a) improved upon this by using a joint-analysis of the BBH, BHNS, and BNS

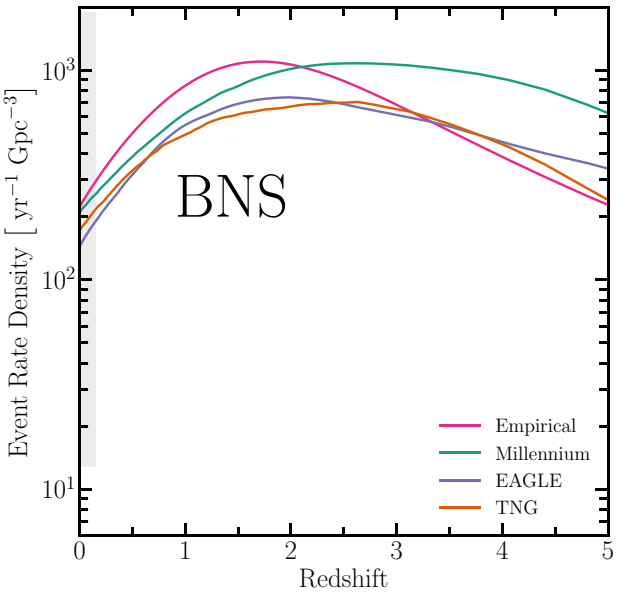

Figure 13. BNS Star merger rate with maximum credible range at $z = 0$ from Abbott et al. (2021a). The $z = 0$ rates are shaded and extended out to $z = 0.15$ for clarity.

populations with multiple population models. As shown in Fig. 14, all predictions lie within the maximum credible region of the models considered, although similar to the BBH merger rate, the empirical and Millennium predictions are at the higher end of this range. The majority of the uncertainty in the rate, this times comes from the `PDB (pair) model`, as can be seen the second panel to the right of Fig. 12. Similar to the BBH rates, the EAGLE and TNG prediction, are better estimators of the observed rate, which is most likely a result

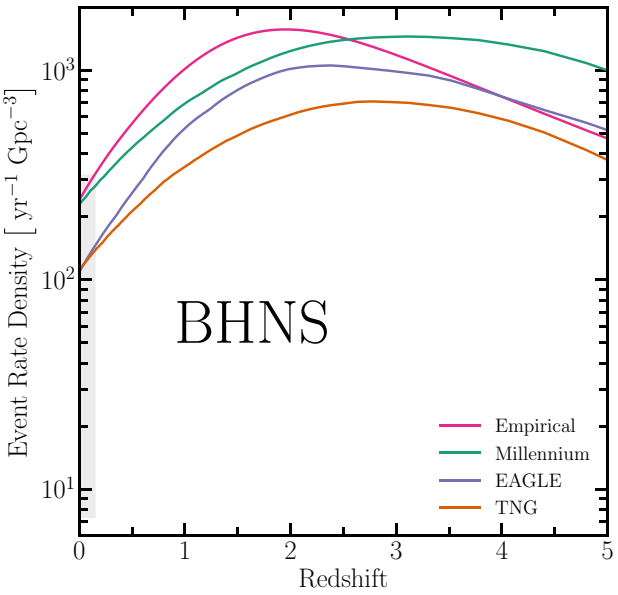

Figure 14. The observed maximum credible range of the BHNS merger rate at $z = 0.2$ from (Abbott et al. 2021a) compared against the TNG, EAGLE, Millennium, and empirical predictions. The $z = 0$ rates are shaded and extended out to $z = 0.15$ for clarity.

of the low metal-poor SFR since black hole formation is dependent on the metallicity of the star formation environment (Mapelli 2021). However, the difference is more pronounced in the BBH rate than the BHNS rate, which agrees with the finding of Drozda et al. (2020) and Broekgaarden et al. (2021b) that show a stronger influence of the stellar physics on the BHNS rate than the star formation environment. The interplay between the cosmic BBH, BHNS, and BNS rates is essential in finding the exact origin of the high black hole formation estimation, but requires further investigation into the influence of the remnant mass determination, mass transfer efficiency, and natal kick.

6 DISCUSSION

6.1 Combined rates analysis

Individually, each transient rate prediction only provides limited information about the different factors that affect it, but taken together it becomes possible to disentangle these influences. To this end, we have performed a reduced χ^2 calculation on the electromagnetic event rates with observation available expect the LGRB rates. The reason for this exclusion is the fact that the geometrical parameters for the observed rate normalization are fitted using the same metallicity distribution and a similar CSFRD as our empirical prescription. They will therefore be biased towards the empirical CSFRD.

Looking at the combined reduced χ^2 of the electromagnetic transients in Table 3, the TNG simulation has the closest χ^2 to 1 with a value of 0.86, followed by a reduced χ^2 of 0.74 by the EAGLE simulation, while the empirical and Millennium predictions have reduced χ^2 of 0.58 and 0.51, respectively. Although the TNG simulation provides the best match to the data, the limited difference in reduced χ^2 values do not allow us to distinguish between the predictions.

The compact objects are excluded in the χ^2 calculation, because there is no robust method to include the credible intervals without knowing their distributions. Instead, we look at these rates qualitatively by considering the population models in Abbott et al. (2021a) with each having its advantages and disadvantages that can drastically alter the observed rates. For example, the fiducial BBH population model (`PP`) evolves over redshift, but does not consider the neutron star masses as part of the same population. On the other hand, the `PDB (ind)` model fits the black hole and neutron star masses, but assumes a non-evolving merger rate over redshift. To show the influence of these assumptions, we showed in Fig. 12 the rates for each population model and compared them against the predicted GW rates in Section 5.5. Here, we consider all GW transients simultaneously and, while the BNS does not provide additional constraints due to the limited observations and, thus, a wide credible interval, we see that the Millennium simulation and empirical prescription overestimate the BBH and BHNS merger rates for the majority of the population models. The EAGLE and TNG predictions, on the other hand, best approximate the observed BBH, BHNS, and BNS merger rates independently of the used population model. This difference is most likely caused by the metallicity distributions and differences in CSFRD. The fact that even these BBH predictions are outside the 90 per cent credible interval for some population models indicates that the BBH rate is overestimated by BPASS, as discussed in Section 5.5.1.

Because the CSFRD of the Millennium simulation aligns with SFR observations at $z < 2$, short delay time events, such as PISNe and CCSNe, are reasonably well predicted at these redshift. However, at higher redshift its CSFRD does not align with SFR observations and the estimated PISN and CCSN rates deviate from the other predictions, which is not taken into account in our χ^2 calculation due to the limited rate observations in this redshift regime. On the other hand, metallicity independent event types with long delay times, such as Type Ia and BNS, do align with observations, which indicates that the total amount of stellar material formed over the history of the universe is correct. Together with the SFR observations misalignment, this indicated that the Millennium CSFRD distribution over redshift is incorrect. Further motivation for the CSFRD misalignment at high redshift comes from metallicity-dependent events, like the BBH and BHNS, which show that the SFR at early times, when there most low-metallicity star formation takes place, is too high resulting in overestimated cosmic rates. This is further motivated by the short delay time and metallicity dependent LGRB rate, whose shape over redshift does not align with observations and peaks at an higher redshift than observed. In summary, the total star formation of the Millennium simulation is correct, but its distribution over redshift and metallicity evolution result in transient rates that deviate from observations.

The empirical CSFRD solves the SFR observation misalignment, but still has a significantly different metallicity distribution over redshift than the simulations, as shown in Fig. 3. Its slow metallicity increase over redshift leads to the overestimation of the BBH and BHNS merger rates, since the low-metallicity star formation at early times is a primary indicator for the BBH rates (Neijssel et al. 2019). The EAGLE and TNG simulations, on the other hand, are able to better estimate the observed BBH and BHNS rates due to faster enrichment in the early universe, even when considering an evolving BBH merger rate. Although subject to model uncertainties (See Section 6.2), this means that more detailed observations of the BHNS and BBH rates can be used to constraint the metallicity-specific CSFRD at high redshift, where observations of metallicity-specific SFRs are limited, providing us with a more complete understanding of the Universe.

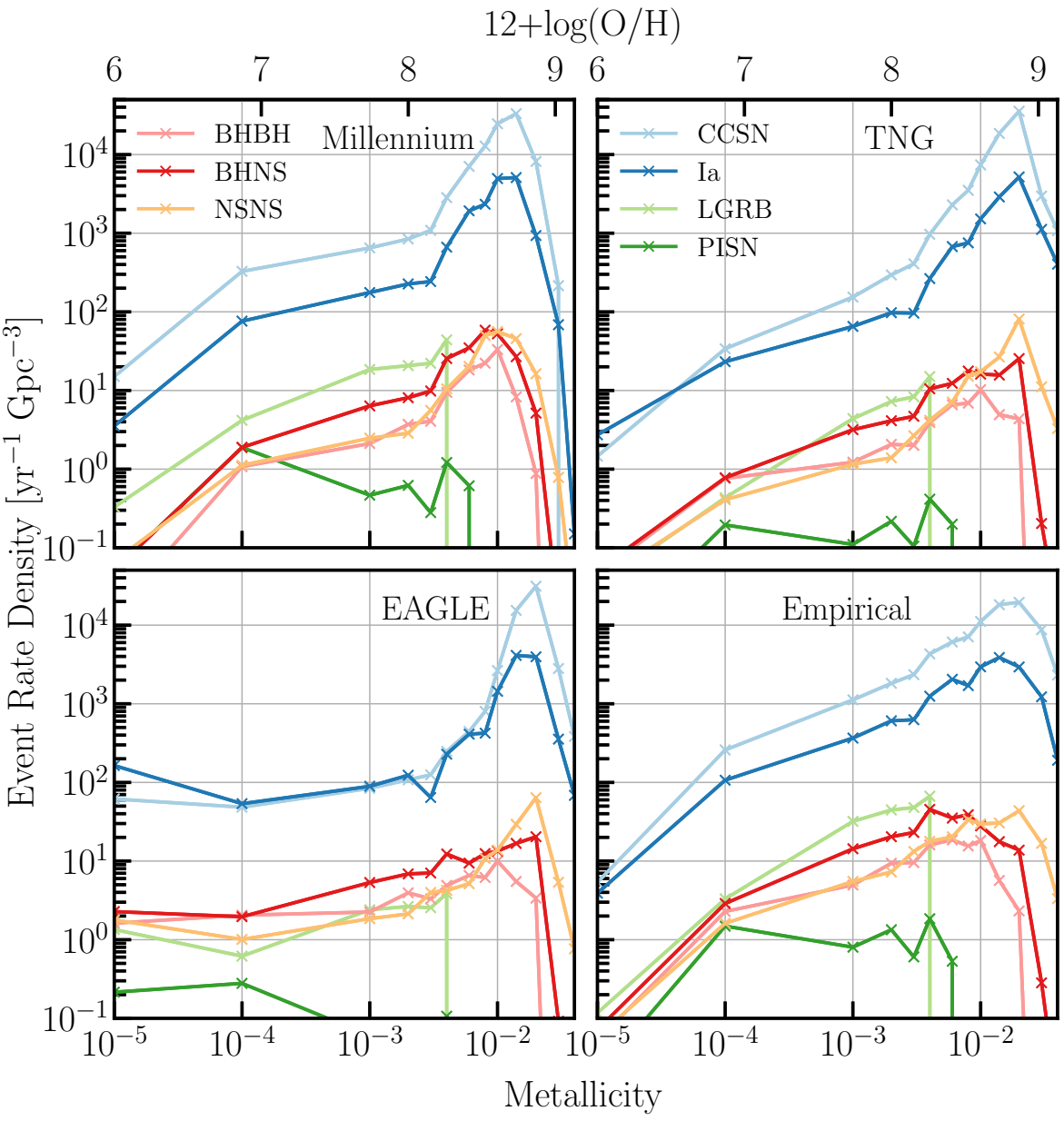

Figure 15. The event rate distribution at $z = 0$ over metallicity for each of the four environment prescriptions. × mark the locations of the BPASS metallicities at which the event rate is calculated. The transformation from metallicity to the O/H ratio is performed using the method in Chrimes et al. (2020).

6.2 Caveats in the estimations

While the EAGLE and TNG simulations are able to reduce the BBH and BHNS rates compared to the empirical and Millennium CSFRD predictions, the estimates remain high, since only isolated binary formation is considered. In reality, a mixture of isolated systems and dynamical interactions in globular clusters, young stellar clusters, nuclear clusters, isolated triples, and systems in active galactic nuclei discs could contribute to the total cosmic merger rates (Santoliquido et al. 2020b; Bouffanais et al. 2021; Gallegos-Garcia et al. 2021; Zevin et al. 2021; and references therein for dynamical interactions). Consequently, even when considering the EAGLE and TNG simulations, the BBH and BHNS rates are high and have to be reduced further. This can be achieved by altering the natal kick, mass transfer efficiency, or common envelope prescription, as described in Section 5.5.1, and possible differences in mass distributions could identify areas of improvement (Mapelli et al. 2019; Ghodla et al. 2021). Especially, as the distribution of masses and spins become available with more observations from the LIGO/VIRGO/KAGRA collaboration, they provide an additional window and new constraints for the formation of binary compact objects, which can be compared against binary population synthesis models, since formation pathways can leave an imprint on the observed population (Neijssel et al. 2019; Arca Sedda et al. 2020; van Son et al. 2021; Bavera et al. 2021b). Furthermore, we would like to point out that in BPASS v2.2.1, the merger time for compact objects is calculated using the mean of a collection of systems instead of each individual system. This could result in more systems merging within the Hubble time that otherwise would not. The individual calculation will be implemented in a future version of BPASS.

Besides the overestimation of the BHNS and BBH rates, the EAGLE and TNG simulations have high Type Ib/c fractions at $z = 0$ compared to the empirical and Millennium predictions due to the higher mean metallicity resulting in stronger stellar winds (e.g. Vink et al. 2001). Moreover, they also are significantly higher than observed by Shivvers et al. (2017) and Perley et al. (2020) indicating too high a typical metallicity at low redshift. Additionally, the short delay-time low-metallicity dependent PISN and LGRB rates are underestimated compared to observations, and from the lower Type Ib/c fraction from the Millennium and empirical CSFRD, which have a lower mean metallicity near $z = 0$. Together, these results indicate that either the metallicity is too high at these redshifts, or the strength of the stellar winds is too high, both resulting in more Type Ib/c and less PISN and LGRBs. It is, however, important to mention that available observations for the Type Ib/c fractions, PISN and LGRB rates are currently limited, but that the continuation of surveys from the Zwicky Transient Facility (Perley et al. 2020) and ATLAS (Smith et al. 2020) will provide better constraints on the Type Ib/c fractions and SLSN observations, while next generation observational facilities, such as THESEUS, will be able to detect large samples of GRBs at $z > 6$ (Tanvir et al. 2021).

With these future observations, it might become possible to distinguish between the similar EAGLE and TNG predictions and provide us with more understanding of the metallicity at high redshift. Moreover, the distributions of event rates at $z = 0$ over metallicity, shown in Fig. 15, is another method to constrain the CSFRD and metallicity evolution. The distributions are all relatively similar, except for the EAGLE simulation, which stands out due to relative high event rates originating from regions of star formation with a metallicity below $Z = 5 \times 10^{-3}$. A possible explanation might be a larger and more equal spread of star formation over metallicity in the EAGLE CSFRD, although Fig. 3 does not provide a clear answer to this question, since the distributions of the EAGLE and TNG look similar at low redshift.

6.3 Uncertainties

There are three main sources of uncertainty in this work: the interference of volumetric rates from observations, the cosmological simulations, and the stellar modelling. We have already touched upon a variety of uncertainties in observations, since they are essential in testing our predictions, but observations at high redshift remain limited and complex, although future surveys will allow for better constraints.

The stellar models used in creating the DTDs used in their study are from BPASS. The uncertainties inherent in the assumed physics within these stellar models and the population synthesis undertaken to combine them is common to all such codes. For example, within BPASS, the Type Ia rate is dominated by single degenerate events, while Ruiter et al. (2009) and Mennekens et al. (2010) predict the double degenerate channel to be dominant. The balance between these pathways depends on mass-loss rates, metallicity, and binary fraction. Ruiter et al. (2009) only looks at a metallicity of $Z = 0.02$ and a binary fraction of 50 per cent. Mennekens et al. (2010) uses the same metallicity, but with a binary fraction of 100 per cent and alterations to the mass transfer efficiencies. Moreover, BPASS does not include the effects of magnetic wind braking, and its inclusion might shift the Type Ia rate (Eldridge et al. 2017; Stanway & Eldridge 2018). These inherent uncertainties in the assumed physics of the stellar models propagate to uncertainties in the predicted transient rates. None the less, we note that the BPASS results have been validated and tested against a wide range of observations beyond just astrophysical transients providing confidence in the predicted DTDs and they are therefore sufficiently accurate to study the large scale trends presented in this work (Eldridge et al. 2017; Stanway & Eldridge 2018, and references therein).

The final area of uncertainty comes from the cosmological simulations. Due the age of the semi-analytical Millennium simulation, it is unable to reproduce several observational constraints (Croton et al. 2006; Oliver et al. 2010; Wang et al. 2019; Lu et al. 2014) and the cosmic rates. The newer hydrodynamic simulations, on the other hand, are able to reproduce a number of observed distributions (see Schaye et al. 2015; Crain et al. 2015; Springel et al. 2018; Nelson et al. 2018; Pillepich et al. 2018b; Naiman et al. 2018; Marinacci et al. 2018) and have better estimates for the cosmic transients rates due to the presence of an SFH and metallicity evolution per galaxy. These are significant benefits of the cosmological simulations compared to the empirical prescription, but they do have some drawbacks. The detail of the large-scale cosmological simulations does not always provide information about the structure and metallicity distribution within the galaxy limiting us to the average metallicity of the galaxy. In reality, the centre and outer regions of galaxies have different abundances (Metha & Trenti 2020), primarily impacting the metallicity dependent rates. Metha, Cameron & Trenti (2021) has shown that including this detail from the Illustris-TNG simulation instead of their mean galaxy metallicity, the BPASS combined LGRB rates match observations.

Furthermore, the metallicity evolution of the cosmological simulations is formed through enrichment processes, such as SN feedback. To account for these processes, internal definitions for different SN types are assumed. For the TNG simulation, these align with observations as shown by Naiman et al. (2018), but are different than predicted by the BPASS models. While the Millennium and EAGLE simulations do not have explicit SN rates, they do use prescriptions that depend on the fraction of massive stars ending their life in a stellar explosion by which they determine the metallicity evolution and stellar growth of galaxies in the simulations (Katsianis et al. 2017; Croton et al. 2006). The predictions using the BPASS models can lead to a different stellar rate, as with the TNG simulation, and therefore alter the enrichment in the simulation. Thus, for a self-consistent model, the SNe feedback would have to be modelled using the BPASSS SN rates.

There are two more elements of the simulations that influence the outcome of the predicted rates. First of all, the internal star formation in the TNG, EAGLE, and Millennium simulations assume a Chabrier IMF (De Lucia & Blaizot 2007; McAlpine et al. 2016; Pillepich et al. 2018b), while the BPASS DTDs used originate from a Kroupa IMF. This discrepancy could result in a deviation in the predicted rates, but the difference would be small since the observational correction from luminosity to SFR between the Kroupa and Chabrier IMF is minimal (Madau & Dickinson 2014). The second internal component is the assumed cosmology in the simulation. While some hydrodynamic simulations are completely scale free and independent of the Hubble parameter, more sophisticated simulations require absolute values for processes, such as cooling and SN feedback (Croton 2013). These dependencies cannot be removed as we have done with the volume and will introduce variations in the predicted rates due to the cosmology. However, its influence is small, especially since the cosmologies from the EAGLE and TNG simulations are similar to the assumed value in this paper. Since the Millennium simulation is a semi-analytical model, it does not suffer the same dependence.

7 CONCLUSION

In this paper, we have predicted electromagnetic and GW cosmic transient rates using detailed stellar models from BPASS and four prescriptions of the star-forming environment from well-known cosmological simulations. These include an empirical prescription and three numerical models originating from the MilliMillennium, EAGLE, and Illustris-TNG simulations, which provide detailed SFH and metallicity evolution for each simulated galaxy over the history of the universe. These additional details lead to significantly different cosmic transient rate prediction, which we compared against observations and against each other, focusing on the difference between the simulations and the empirical prescription.

(i) There can be up to an order of magnitude difference between the predicted rates from the empirical model and those from the cosmological simulations. While most event types differ a factor of 2, the predicted rates are significantly altered when the delay-times distribution for the events are extended and/or when the rates are highly metallicity dependent; up to a factor of 2.38 for the BBH transient rate, and up to 9.66 for the LGRB rates. This result suggests that care should be taken in choosing which cosmic SFH to use, especially how the metallicity evolution is modelled when predicting transient rates. Those that are most sensitive are events with long, >1 Gyr, delay times and strong dependence on metallicity.

(ii) The cosmological simulations have metallicity-specific CSFRD with reduced early star formation and faster enrichment than the empirical prescription. Of the SFH considered, the Millennium simulation has the most uniquely shaped CSFRD, which does not agree with SFR observations, and has a near constant mean metallicity over redshift resulting in distinct cosmic transient rates. Compared to observations, the predictions from the Millennium simulation agree with the observations for the Type Ia, CCSN, PISN, and BNS rates, but overestimate the BHNS and BBH rates. The TNG and EAGLE simulation solve this overestimation with an increasing mean metallicity evolution and a observationally constraint CSFRD resulting in BHNS and BBH rates closer to observation irrespective of the assumed black hole and neutron star population model, while at the same time the Type Ia, CCSN, and BNS rates are minimally affected. However, the PISN and LGRB rates do decrease significantly due to the higher metallicity, but the number of observations are limited or hard to constrain. Moreover, the inclusion of star formation on a per simulation particle basis instead of mean galaxy metallicity can solve the discrepancy between current observations and our LGRB prediction from the TNG simulation (Metha et al. 2021). Future observations, like long-term deep transient surveys (Moriya et al. 2021) and next-generation observational facilities, such as THESEUS (Tanvir et al. 2021), will put better constraints on the SLSN and LGRB rates, and through these events a better understanding of the metallicity evolution over redshift (Fryer et al. 2021).

(iii) We find that the predictions of the empirical prescription, based on the CSFRD from Madau & Dickinson (2014) and metallicity evolution from Langer & Norman (2006), align well with observed CCSN and Type Ia rates from multiple surveys. Moreover, the predicted fraction of Type Ib/c at $z = 0$ of 0.71 is similar to 0.722 found by Perley et al. (2020), and the predicted LGRB, PISN, and BNS rates align well, although the observations for the LGRB and PISN are not well constrained. Furthermore, the BHNS and BBH rates are significantly overestimated compared to observations up to almost an order of magnitude, which can be a result of our assumptions in stellar physics, mass transfer, common envelope evolution, or natal kick (Santoliquido et al. 2020a; du Buisson et al. 2020; Marchant et al. 2021; Bavera et al. 2021b; Olejak & Belczynski 2021; Olejak et al. 2021; van Son et al. 2020; Igoshev et al. 2021; Klencki et al. 2021; Belczynski et al. 2021).

(iv) The additional detail in the metallicity-specific CSFRD provided by the TNG and EAGLE simulations result in good cosmic rate estimations across the board, but especially improves upon the BHNS and BBH rates compared to the standard empirical prescription. These new cosmological simulations have been improved to fit a variety of observations. The semi-analytical models from the Millennium simulation, on the other hand, are older and unable to match the observed CSFRD over redshift. Together with the near flat metallicity evolution, it results in significant overestimation of the BBH and BHNS rate with minimal changes in the other rates compared to the empirical prescription.

(v) In this paper, we have only considered isolated binary evolution for the BBH and BHNS rates. The Universe has more than one way to make compact object mergers happen with the contribution of each pathway, such as isolated and dynamic formation still being undetermined. This means that even the better rate estimations from the EAGLE and TNG simulations for the BBH and BHNS rates are likely still too high. Adjustment of the CEE or natal kick, or inclusion of pulsation pair instability might be necessary for more accurate rate predictions.

All together, we find that the EAGLE and TNG simulation provide the best metallicity-specific CSFRD based on the predicted cosmic rates for electromagnetic and GW transients. The additional detail provides clear benefits over the empirical prescription, closer matching the irregular and complex metallicity and SFR evolution of the real Universe, constraining environmental and evolutionary parameters. As the observational constraints improve over the coming decades for the SFH and cosmic transients rates, we expect the true complexity of their variation over redshift to be revealed.

ACKNOWLEDGEMENTS

We would like to thank the anonymous referee for their useful comments and suggestions that helped improve this paper. MMB, JJE, and HFS acknowledge support by the University of Auckland and funding from the Royal Society Te Aparāngi of New Zealand Marsden Grant Scheme. ERS acknowledges support by the University of Warwick and funding from the UK Science and Technology Facilities Council (STFC) through Consolidated Grant ST/T000406/1. We are grateful to the developers of PYTHON, MATPLOTLIB (Hunter 2007), NUMPY (Harris et al. 2020), and PANDAS (Reback et al. 2020).

The BPASS project makes use of New Zealand eScience Infrastructure (NeSI) high performance computing facilities. New Zealand's national facilities are funded jointly by NeSI's collaborator institutions and through the Ministry of Business, Innovation & Employment's Research Infrastructure programme.

DATA AVAILABILITY

Code and data products underlying this work are available at the organizational github[1] and website.[2]

[1] https://github.com/UoA-Stars-And-Supernovae
[2] www.bpass.auckland.ac.nz

REFERENCES

Abbott B. P. et al., 2016, Phys. Rev. Lett., 116, 061102
Abbott B. P. et al., 2017, ApJ, 848, L12
Abbott R. et al., 2021, ApJ, 913, L7
Abbott R., The LIGO Scientific Collaboration, The Virgo Collaboration, The KAGRA Scientific Collaboration, 2021a, preprint (astro-Ph/2111.03634)
Abbott R. et al., 2021b, ApJ, 915, L5
Ade P. A. R. et al., 2015, A&A, 594, 63
Aghanim N. et al., 2020, A&A, 641, A6
Arca Sedda M., Mapelli M., Spera M., Benacquista M., Giacobbo N., 2020, ApJ, 894, 133
Artale M. C., Mapelli M., Giacobbo N., Sabha N. B., Spera M., Santoliquido F., Bressan A., 2019, MNRAS, 487, 1675
Artale M. C., Mapelli M., Bouffanais Y., Giacobbo N., Pasquato M., Spera M., 2020, MNRAS, 491, 3419
Bavera S. S. et al., 2022, A&A, 657, L8
Bavera S. S. et al., 2021b, A&A, 647, A153
Bazin G. et al., 2009, A&A, 499, 653
Behroozi P. S., Wechsler R. H., Conroy C., 2013, ApJ, 770, 57
Belczynski K. et al., 2016, A&A, 594, A97
Belczynski K. et al., 2018, preprint (astro-Ph/1812.10065)
Belczynski K. et al., 2020, A&A, 636, A104
Belczynski K. et al., 2022, ApJ, 925, 69
Blanc G. et al., 2004, A&A, 423, 881
Botticella M. T. et al., 2008, A&A, 479, 49
Bouffanais Y., Mapelli M., Santoliquido F., Giacobbo N., Di Carlo U. N., Rastello S., Artale M. C., Iorio G., 2021, MNRAS, 507, 5524
Broekgaarden F. S. et al., 2021a, preprint(astro-Ph/2112.05763)
Broekgaarden F. S. et al., 2021b, MNRAS, 508, 5028
Calzetti D., Armus L., Bohlin R. C., Kinney A. L., Koornneef J., Storchi-Bergmann T., 2000, ApJ, 533, 682
Cappellaro E., Evans R., Turatto M., 1999, A&A, 351, 459
Cappellaro E. et al., 2005, A&A, 430, 83
Cappellaro E. et al., 2015, A&A, 584, A62
Chrimes A. A., Stanway E. R., Eldridge J. J., 2020, MNRAS, 491, 3479
Chruslinska M., Nelemans G., 2019, MNRAS, 488, 5300
Chruslinska M., Belczynski K., Klencki J., Benacquista M., 2018, MNRAS, 474, 2937
Chruslinska M., Nelemans G., Belczynski K., 2019, MNRAS, 482, 5012
Chu Q., Yu S., Lu Y., 2021, MNRAS, 509, 1557
Cooke J. et al., 2012, Nature, 491, 228
Crain R. A. et al., 2015, MNRAS, 450, 1937
Croton D., 2013, PASA, 30, e052
Croton D. J. et al., 2006, MNRAS, 365, 11
Cucchiara A. et al., 2011, ApJ, 736, 7
Dabrowny M., Giacobbo N., Gerosa D., 2021, Scienze Fisiche e Naturali, 32, 665
Dahlen T., Strolger L.-G., Riess A. G., 2008, ApJ, 681, 462
Dahlen T., Strolger L.-G., Riess A. G., Mattila S., Kankare E., Mobasher B., 2012, ApJ, 757, 70
de Jager C., Nieuwenhuijzen H., van der Hucht K. A., 1988, A&AS, 72, 259
Dessart L., Hillier D. J., Waldman R., Livne E., Blondin S., 2012, MNRAS, 426, L76
De Donder E., Vanbeveren D., 1998, A&A, 333, 557
De Lucia G., Blaizot J., 2007, MNRAS, 375, 2
Dilday B. et al., 2010, ApJ, 713, 1026
Dolag K., Borgani S., Murante G., Springel V., 2009, MNRAS, 399, 497
Dominik M., Belczynski K., Fryer C., Holz D. E., Berti E., Bulik T., Mandel I., O'Shaughnessy R., 2013, ApJ, 779, 72
Drozda P., Belczynski K., O'Shaughnessy R., Bulik T., Fryer C. L., 2020, preprint(astro-Ph/2009.06655)
du Buisson L. et al., 2020, MNRAS, 499, 5941
Eggleton P. P., 1971, MNRAS, 151, 351
Eldridge J. J., Tout C. A., 2004, MNRAS, 353, 87
Eldridge J. J., Izzard R. G., Tout C. A., 2008, MNRAS, 384, 1109
Eldridge J. J., Langer N., Tout C. A., 2011, MNRAS, 414, 3501
Eldridge J. J., Fraser M., Smartt S. J., Maund J. R., Crockett R. M., 2013, MNRAS, 436, 774
Eldridge J. J., Stanway E. R., Xiao L., McClelland L. A., Taylor G., Ng M., Greis S. M., Bray J. C., 2017, PASA, 34, e058
Eldridge J. J., Stanway E. R., Tang P. N., 2019, MNRAS, 482, 870
Farmer R., Renzo M., de Mink S. E., Marchant P., Justham S., 2019, ApJ, 887, 53
Filippenko A. V., 1997, ARA&A, 35, 309
Fowler W. A., Hoyle F., 1964, ApJS, 9, 201
Frohmaier C. et al., 2019, MNRAS, 486, 2308
Frohmaier C. et al., 2021, MNRAS, 500, 5142
Fryer C. L., Woosley S. E., Heger A., 2001, ApJ, 550, 372
Fryer C. L., Lien A. Y., Fruchter A., Ghirlanda G., Hartmann D., Salvaterra R., Upton Sanderbeck P. R., Johnson J. L., 2022, ApJ, 929, 17
Gal-Yam A. et al., 2009, Nature, 462, 624
Gallegos-Garcia M., Berry C. P. L., Marchant P., Kalogera V., 2021, ApJ, 922, 110
Ghodla S., van Zeist W. G. J., Eldridge J. J., Stevance H. F., Stanway E. R., 2022, MNRAS, 511, 1201
Giacobbo N., Mapelli M., 2018, MNRAS, 480, 2011
Gilbank D. G., Baldry I. K., Balogh M. L., Glazebrook K., Bower R. G., 2010, MNRAS, 405, 2594
Gomez S. et al., 2019, ApJ, 881, 87
Graur O., Maoz D., 2013, MNRAS, 430, 1746
Graur O. et al., 2011, MNRAS, 417, 916
Graur O. et al., 2014, ApJ, 783, 28
Graur O., Bianco F. B., Modjaz M., 2015, MNRAS, 450, 905
Han Z.-W., Ge H.-W., Chen X.-F., Chen H.-L., 2020, Res. A&A, 20, 161
Harris C. R. et al., 2020, Nature, 585, 357
Heger A., Woosley S. E., 2002, ApJ, 567, 532
Heger A., Fryer C. L., Woosley S. E., Langer N., Hartmann D. H., 2003, ApJ, 591, 288
Hobbs G., Lorimer D. R., Lyne A. G., Kramer M., 2005, MNRAS, 360, 974
Horesh A., Poznanski D., Ofek E. O., Maoz D., 2008, MNRAS, 389, 1871
Howell D. A., 2011, Nat. Commun., 2, 350
Howell D. A., 2017, Superluminous Supernovae. In Handbook of Supernovae. Springer, Cham, p. 431
Hunter J. D., 2007, Comput. Sci. Eng., 9, 90
Hurley J. R., Tout C. A., Pols O. R., 2002, MNRAS, 329, 897
Igoshev A. P., Chruslinska M., Dorozsmai A., Toonen S., 2021, MNRAS, 508, 3345
Inserra C. et al., 2013, ApJ, 770, 128
Ivanova N. et al., 2013, A&AR, 21, 59
Karim A. et al., 2011, ApJ, 730, 61
Kasen D., Bildsten L., 2010, ApJ, 717, 245
Katsianis A. et al., 2017, MNRAS, 472, 919
Klencki J., Nelemans G., Istrate A. G., Chruslinska M., 2021, A&A, 645, 27
Kozyreva A., Blinnikov S., 2015, MNRAS, 454, 4357
Kroupa P., 2001, MNRAS, 322, 231
Kruckow M. U., Tauris T. M., Langer N., Kramer M., Izzard R. G., 2018, MNRAS, 481, 1908
Lamberts A. et al., 2018, MNRAS, 480, 2704
Langer N., 2012, ARA&A, 50, 107
Langer N., Norman C. A., 2006, ApJ, 638, L63
Lemson G., the Virgo Consortium, 2006, preprint (astro-ph/0608.019)
Li W. et al., 2011a, MNRAS, 412, 1441
Li W., Chornock R., Leaman J., Filippenko A. V., Poznanski D., Wang X., Ganeshalingam M., Mannucci F., 2011b, MNRAS, 412, 1473
Lu Y. et al., 2014, ApJ, 795, 123
Madau P., Dickinson M., 2014, ARA&A, 52, 415
Madau P., Fragos T., 2017, ApJ, 840, 39
Madgwick D. S., Hewett P. C., Mortlock D. J., Wang L., 2003, ApJ, 599, L33
Mandel I., Broekgaarden F. S., 2022, Living Rev Relativ, 25, 1
Mannucci F., Della Valle M., Panagia N., Cappellaro E., Cresci G., Maiolino R., Petrosian A., Turatto M., 2005, A&A, 433, 807
Maoz D., Mannucci F., 2012, PASA, 29, 447
Maoz D., Mannucci F., Nelemans G., 2014, ARA&A, 52, 107

Mapelli M., 2021, Formation Channels of Single and Binary Stellar-Mass Black Holes. Handbook of Gravitational Wave Astronomy. Springer, Singapore
Mapelli M., Giacobbo N., 2018, MNRAS, 479, 4391
Mapelli M., Giacobbo N., Ripamonti E., Spera M., 2017, MNRAS, 472, 2422
Mapelli M., Giacobbo N., Santoliquido F., Artale M. C., 2019, MNRAS, 487, 2
Marchant P., Pappas K. M. W., Gallegos-Garcia M., Berry C. P. L., Taam R. E., Kalogera V., Podsiadlowski P., 2021, A&A, 650, A107
Marinacci F. et al., 2018, MNRAS, 480, 5113
Matthews A. M., Condon J. J., Cotton W. D., Mauch T., 2021, ApJ, 914, 126
Mattila S. et al., 2012, ApJ, 756, 111
McAlpine S. et al., 2016, Astron. Comput., 15, 72
Melinder J. et al., 2012, A&A, 545, A96
Mennekens N., Vanbeveren D., De Greve J. P., De Donder E., 2010, A&A, 515, A89
Metha B., Trenti M., 2020, MNRAS, 495, 266
Metha B., Cameron A. J., Trenti M., 2021, MNRAS, 504, 5992
Moe M., Di Stefano R., 2017, ApJS, 230, 15
Moe M., Kratter K. M., Badenes C., 2019, ApJ, 875, 61
Moriya T. J. et al., 2019, ApJS, 241, 16
Moriya T. J. et al., 2021, ApJ, 908, 249
Naiman J. P. et al., 2018, MNRAS, 477, 1206
Neijssel C. J. et al., 2019, MNRAS, 490, 3740
Neill J. D. et al., 2006, ApJ, 132, 1126
Nelson D. et al., 2018, MNRAS, 475, 624
Nelson D. et al., 2019, Comput. Astrophys., 6, 2
Nugis T., Lamers H. J. G. L. M., 2000, A&A, 360, 227
Okumura J. E. et al., 2014, PASJ, 66, 49
Olejak A., Belczynski K., 2021, ApJ, 921, L2
Olejak A., Belczynski K., Ivanova N., 2021, A&A, 651, 17
Oliver S. et al., 2010, MNRAS, 405, 2279
Paczyński B., 1971, ARA&A, 9, 183
Pain R. et al., 2002, ApJ, 577, 120
Perley D. A. et al., 2016, ApJ, 817, 7
Perley D. A. et al., 2020, ApJ, 904, 35
Perrett K. et al., 2012, ApJ, 144, 59
Pescalli A. et al., 2016, A&A, 587, A40
Peters P. C., 1964, Phys. Rev., 136, B1224
Petrushevska T. et al., 2016, A&A, 594, A54
Pillepich A. et al., 2018a, MNRAS, 473, 4077
Pillepich A. et al., 2018b, MNRAS, 475, 648
Podsiadlowski P., Joss P. C., Hsu J. J. L., 1992, ApJ, 391, 246
Prajs S. et al., 2017, MNRAS, 464, 3568
Quimby R. M., Yuan F., Akerlof C., Wheeler J. C., 2013, MNRAS, 431, 912
Rakavy G., Shaviv G., 1967, ApJ, 148, 803
Reback J. et al., 2020, Pandas-dev/pandas: Pandas 1.0.3. Zenodo
Renzo M., Farmer R., Justham S., Götberg Y., de Mink S. E., Zapartas E., Marchant P., Smith N., 2020, A&A, 640, A56
Rodighiero G. et al., 2010, A&A, 518, L25
Rodney S. A., Tonry J. L., 2010, ApJ, 723, 47
Rodney S. A. et al., 2014, AJ, 148, 13
Rodriguez-Gomez V. et al., 2015, MNRAS, 449, 49
Ruiter A. J., Belczynski K., Fryer C. L., 2009, ApJ, 699, 2026
Ruiter A. J., Belczynski K., Sim S. A., Hillebrandt W., Fryer C. L., Fink M., Kromer M., 2011, MNRAS, 417, 408
Salpeter E. E., 1955, ApJ, 121, 161
Santoliquido F., Mapelli M., Giacobbo N., Bouffanais Y., Artale M. C., 2021, MNRAS, 502, 4877
Santoliquido F., Mapelli M., Bouffanais Y., Giacobbo N., Di Carlo U. N., Rastello S., Artale M. C., Ballone A., 2020b, ApJ, 898, 152
Schaye J. et al., 2015, MNRAS, 446, 521
Schmidt M., 1959, ApJ, 129, 243
Shivvers I. et al., 2017, PASP, 129, 054201
Smartt S. J., Eldridge J. J., Crockett R. M., Maund J. R., 2009, MNRAS, 395, 1409
Smith N., Li W., Filippenko A. V., Chornock R., 2011, MNRAS, 412, 1522
Smith K. W. et al., 2020, PASP, 132, 085002
Somerville R. S., Primack J. R., Faber S. M., 2001, MNRAS, 320, 504
Springel V., White S., Tormen G., Kauffmann G., 2001, MNRAS, 328, 726
Springel V. et al., 2005, Nature, 435, 629
Springel V. et al., 2018, MNRAS, 475, 676
Stanway E. R., Eldridge J. J., 2018, MNRAS, 479, 75
Stanway E. R., Hoskin M. J., Lane M. A., Brown G. C., Childs H. J., Greis S. M., Levan A. J., 2018, MNRAS, 475, 1829
Stevance H. F., Eldridge J. J., Stanway E., 2020, J. Open Source Softw., 5, 1987
Stevenson S., Sampson M., Powell J., Vigna-Gómez A., Neijssel C. J., Szécsi D., Mandel I., 2019, ApJ, 882, 121
Strolger L.-G., 2003, PhD thesis, Univ. Michigan
Strolger L.-G. et al., 2015, ApJ, 813, 93
Strolger L.-G., Rodney S. A., Pacifici C., Narayan G., Graur O., 2020, ApJ, 890, 140
Tang P. N., Eldridge J. J., Stanway E. R., Bray J. C., 2020, MNRAS, 493, L6
Tanvir N. R. et al., 2021, Experimental Astronomy, 52, 219
Taylor M. et al., 2014, ApJ, 792, 135
Terreran G. et al., 2017, Nat Astron, 1, 713
Toffano M., Mapelli M., Giacobbo N., Artale M. C., Ghirlanda G., 2019, MNRAS, 11, 1
Tonry J. L. et al., 2003, ApJ, 594, 1
Tout C. A., 2011, Proc. IAU, 7, 44
van Son L. A. C. et al., 2020, ApJ, 897, 100
van Son L. A. C. et al., 2022, ApJ, 931, 17
Vanbeveren D., De Loore C., Van Rensbergen W., 1998, A&AR, 9, 63
Vink J. S., de Koter A., Lamers H. J. G. L. M., 2001, A&A, 369, 574
Wang L., De Lucia G., Fontanot F., Hirschmann M., 2019, MNRAS, 482, 4454
Weinberger R. et al., 2017, MNRAS, 465, 3291
Wiersma R. P. C., Schaye J., Theuns T., Dalla Vecchia C., Tornatore L., 2009, MNRAS, 399, 574
Wilkins S. M., Bouwens R. J., Oesch P. A., Labbé I., Sargent M., Caruana J., Wardlow J., Clay S., 2016, MNRAS, 455, 659
Wilkins S. M., Feng Y., Di Matteo T., Croft R., Lovell C. C., Thomas P., 2018, MNRAS, 473, 5363
Woosley S. E., 2010, ApJ, 719, L204
Woosley S. E., 2017, ApJ, 836, 244
Woosley S. E., Heger A., 2021, ApJ, 912, L31
Woosley S. E., Heger A., Weaver T. A., 2002, Rev. Mod. Phys., 74, 1015
Woosley S. E., Blinnikov S., Heger A., 2007, Nature, 450, 390
Yoon S.-C., 2015, PASA, 32, e015
Yoon S.-C., Woosley S. E., Langer N., 2010, ApJ, 725, 940
Yusof N., Kassima H. A., Hirschi R., Crowther P. A., Schnurr O., Parkerd R. J., Goodwin S. P., 2010, preprint (astro-ph/1012.3649)
Yusof N. et al., 2013, MNRAS, 433, 1114
Zapartas E. et al., 2017, A&A, 601, A29
Zevin M. et al., 2021, ApJ, 910, 152
Zhao W.-C., Xue X.-X., Cao X.-F., 2020, preprint (astro-ph/2009.13808)

APPENDIX: OBSERVATIONS

See Tables A1–A4.

Table A1. The observations used for Type Ia comparison. Adapted from Strolger et al. (2020) with additional observations from Melinder et al. (2012) and Li et al. (2011b), redshift ranges if available, and updated rates for Madgwick et al. (2003) from Graur & Maoz (2013). Uncertainty is split between the statistic and systematic uncertainty. If the separate numbers are available, the latter is in between brackets.

Redshift	Rate	Uncertainty ($10^5\ h^3\ \mathrm{yr}^{-1}\ \mathrm{Gpc}^{-3}$)		Reference
0	0.77	−0.10 (−0.13)	0.10 (0.13)	Li et al. (2011b)
0.01	0.82	−0.26 (NA)	0.26 (NA)	Cappellaro, Evans & Turatto (1999)
0.03	0.82	−0.32 (NA)	0.32 (NA)	Mannucci et al. (2005)
0.025–0.050	0.81	−0.24 (NA)	0.33 (0.04)	Dilday et al. (2010)
0.073	0.71	−0.08 (−0.06)	0.08 (0.10)	Frohmaier et al. (2019)
0.05–0.15	1.60	−0.85 (−0.58)	1.46 (0.58)	Cappellaro et al. (2015)
0.075–0.125	0.76	−0.13 (0.00)	0.15 (0.08)	Dilday et al. (2010)
0.11	1.08	−0.29 (NA)	0.29 (NA)	Strolger (2003)
0.11	0.72	−0.18 (−0.09)	0.08 (0.05)	Graur & Maoz (2013)
0.13	0.58	−0.20 (−0.15)	0.20 (0.15)	Blanc et al. (2004)
0.15	0.93	−0.67 (−0.17)	0.67 (0.67)	Rodney & Tonry (2010)
0.125–0.175	0.90	−0.10 (−0.01)	0.11 (0.10)	Dilday et al. (2010)
0.16	0.41	−0.26 (−0.35)	0.26 (0.17)	Perrett et al. (2012)
0.175–0.225	1.01	−0.09 (−0.02)	0.09 (0.24)	Dilday et al. (2010)
0.2	0.58	−0.23 (NA)	0.23 (NA)	Horesh et al. (2008)
0.25	1.05	−0.76 (−1.02)	1.75 (0.35)	Rodney et al. (2014)
0.15–0.35	1.14	−0.35 (−0.29)	0.38 (0.29)	Cappellaro et al. (2015)
0.225–0.275	1.06	−0.08 (−0.03)	0.09 (0.53)	Dilday et al. (2010)
0.26	0.82	−0.20 (−0.20)	0.20 (0.17)	Perrett et al. (2012)
0.3	0.99	−0.44 (NA)	0.47 (NA)	Botticella et al. (2008)
0.275–0.325	1.27	−0.10 (−0.05)	0.11 (1.15)	Dilday et al. (2010)
0.35	0.99	−0.55 (−0.09)	0.55 (0.55)	Rodney & Tonry (2010)
0.35	1.05	−0.17 (−0.17)	0.17 (0.15)	Perrett et al. (2012)
0.42	1.34	−0.93 (−0.38)	1.22 (0.29)	Graur et al. (2014)
0.44	0.76	−0.39 (−0.35)	0.67 (0.17)	Okumura et al. (2014)
0.45	0.90	−0.44 (−0.12)	0.44 (0.44)	Rodney & Tonry (2010)
0.45	1.05	−0.17 (−0.15)	0.17 (0.12)	Perrett et al. (2012)
0.35–0.55	1.52	−0.38 (−0.47)	0.32 (0.47)	Cappellaro et al. (2015)
0.46	1.40	−0.50 (NA)	0.50 (NA)	Tonry et al. (2003)
0.47	1.22	−0.17 (−0.26)	0.17 (0.38)	Neill et al. (2006)
0.47	2.33	−0.79 (−0.76)	1.08 (4.84)	Dahlen, Strolger & Riess (2008)
0.55	0.93	−0.41 (−0.20)	0.41 (0.41)	Rodney & Tonry (2010)
0.55	1.40	−0.17 (−0.15)	0.17 (0.12)	Perrett et al. (2012)
0.55	1.52	−0.26 (NA)	0.29 (NA)	Pain et al. (2002)
0.62	3.76	−1.66 (−0.82)	2.57 (0.79)	Melinder et al. (2012)
0.65	1.40	−0.15 (−0.17)	0.15 (0.12)	Perrett et al. (2012)
0.55–0.75	2.01	−0.52 (−0.79)	0.55 (0.79)	Cappellaro et al. (2015)
0.65	1.43	−0.50 (−0.23)	0.50 (0.50)	Rodney & Tonry (2010)
0.74	2.30	−1.20 (NA)	0.96 (N.A.)	Graur et al. (2011)
0.75	1.49	−0.55 (−0.55)	0.79 (0.67)	Rodney et al. (2014)
0.75	1.98	−0.61 (−0.41)	0.61 (0.61)	Rodney & Tonry (2010)
0.75	1.69	−0.17 (−0.20)	0.17 (0.15)	Perrett et al. (2012)
0.8	2.45	−0.54 (−0.35)	0.67 (0.17)	Okumura et al. (2014)
0.83	3.79	−0.79 (−1.49)	0.96 (2.13)	Dahlen et al. (2008)
0.85	2.27	−0.64 (−0.47)	0.64 (0.64)	Rodney & Tonry (2010)
0.85	1.66	−0.15 (−0.20)	0.15 (0.17)	Perrett et al. (2012)
0.94	1.31	−0.55 (−0.17)	0.64 (0.38)	Graur et al. (2014)
0.95	2.22	−0.73 (−0.76)	0.73 (0.73)	Rodney & Tonry (2010)
0.95	2.24	−0.23 (−0.35)	0.23 (0.29)	Perrett et al. (2012)
1.05	2.30	−0.82 (−1.20)	0.82 (0.82)	Rodney & Tonry (2010)
1.1	2.16	−0.35 (−0.38)	0.35 (0.29)	Perrett et al. (2012)
1.14	2.06	−0.53 (−0.30)	0.70 (0.30)	Okumura et al. (2014)
1.21	3.85	−0.85 (−0.93)	1.05 (1.11)	Dahlen et al. (2008)
1.23	2.45	−0.82 (N.A.)	0.73 (N.A.)	Graur et al. (2011)
1.25	1.87	−0.64 (−0.67)	0.90 (0.99)	Rodney et al. (2014)
1.59	1.31	−0.64 (−0.26)	0.99 (0.15)	Graur et al. (2014)
1.61	1.22	−0.67 (−0.41)	1.14 (0.55)	Dahlen et al. (2008)
1.69	2.97	−1.08 (N.A.)	1.57 (N.A.)	Graur et al. (2011)
1.75	2.10	−0.87 (−0.82)	1.31 (1.46)	Rodney et al. (2014)
2.25	1.43	−1.11 (−0.70)	2.77 (1.31)	Rodney et al. (2014)

Table A2. The observed CCSN rates from literature. Uncertainty is split between the statistic and systematic uncertainty. If the separate numbers are available, the latter is in between brackets.

Redshift	Rate	Uncertainty ($10^5\ h^3\ \mathrm{yr}^{-1}\ \mathrm{Gpc}^{-3}$)		Reference
0	1.81	−0.20 (−0.44)	0.20 (0.50)	Li et al. (2011b)
0.01	1.25	−0.50 (NA)	0.50 (NA)	Cappellaro et al. (1999)
0.028	2.65	−0.37 (NA)	0.45 (NA)	Frohmaier et al. (2021)
0.03–0.09	3.09	−0.32 (−0.44)	0.32 (0.44)	Taylor et al. (2014)
0.05–0.15	3.29	−1.55 (−1.43)	1.81 (1.43)	Cappellaro et al. (2015)
0.075	3.03	−0.76 (−0.32)	0.96 (0.12)	Graur, Bianco & Modjaz (2015)
0.1–0.5	8.75	−2.74 (−1.66)	3.73 (3.03)	Dahlen et al. (2012)
0.1–0.5	6.21	−1.57 (NA)	2.33 (NA)	Strolger et al. (2015)
0.1–0.5	9.59	−5.19 (−4.23)	8.98 (5.77)	Melinder et al. (2012)
0.15–0.35	3.53	−0.79 (−1.37)	0.79 (1.37)	Cappellaro et al. (2015)
0.21	3.35	−0.99 (−1.05)	1.25 (1.22)	Botticella et al. (2008)
0.26	6.41	−2.04 (NA)	2.33 (NA)	Cappellaro et al. (2005)
0.3	4.14	−0.87 (−0.70)	0.87 (−0.93)	Bazin et al. (2009)
0.4–0.9	8.16	−5.83 (NA)	13.12 (NA)	Petrushevska et al. (2016)
0.5–0.9	10.73	−2.10 (NA)	2.80 (NA)	Strolger et al. (2015)
0.5–0.9	21.55	−4.43 (−4.66)	5.42 (9.33)	Dahlen et al. (2012)
0.5–0.9	18.66	−9.10 (−6.15)	15.45 (10.64)	Melinder et al. (2012)
0.5–1.0	20.12	−15.74 (NA)	28.86 (NA)	Graur et al. (2011)
0.9–1.3	8.95	−1.92 (NA)	3.09 (NA)	Strolger et al. (2015)
0.9–1.3	27.90	−8.16 (−8.16)	10.96 (14.46)	Dahlen et al. (2012)
0.9–1.4	30.03	−17.78 (NA)	33.53 (NA)	Petrushevska et al. (2016)
1.3–1.7	9.48	−3.85 (NA)	5.92 (NA) s	Strolger et al. (2015)
1.4–1.0	31.49	−25.95 (NA)	71.14 (NA)	Petrushevska et al. (2016)
1.7–2.1	9.21	−5.16 (NA)	9.83 (NA)	Strolger et al. (2015)
2.1–2.5	17.99	−10.26 (NA)	19.71 (NA)	Strolger et al. (2015)

Table A3. The observed SLSN Type I rates from literature with the combined statistical and systematic uncertainties are given. Adapted from Frohmaier et al. (2021).

Redshift	Rate	Uncertainty ($h^3\ \mathrm{yr}^{-1}\ \mathrm{Gpc}^{-3}$)		Reference
0.17	102	−38	73	Frohmaier et al. (2021)
0.17	89	−73	215	Quimby et al. (2013)
0–1.6	117	NA	NA	Zhao et al. (2020)
1.13	265	−105	222	Prajs et al. (2017)
2.0–4.0	1118	−559	559	Cooke et al. (2012)
2.5–3.5	1166	−1166	1166	Moriya et al. (2019)

Table A4. The observed Type II rates from literature. Uncertainty is split between the statistic and systematic uncertainty. If the separate numbers are available, the latter is in between brackets.

Redshift	Rate	Uncertainty ($10^5\ h^3\ \mathrm{yr}^{-1}\ \mathrm{Gpc}^{-3}$)		Reference
0	1.15	−0.36 (NA)	0.36 (NA)	Li et al. (2011b)
0.15–0.35	2.01	−0.52 (−0.70)	0.47 (0.70)	Cappellaro et al. (2015)

This paper has been typeset from a TEX/LATEX file prepared by the author.